Seal Capacity, Force Chains, and Percolation in Silt-Clay Mixtures

Abhishek Bihani[1,2], Hugh Daigle[1,2]

[1]Hildebrand Department of Petroleum and Geosystems Engineering, The University of Texas at Austin, Austin, Texas, USA; [2]Center for Subsurface Energy and the Environment, University of Texas at Austin, Austin, Texas, USA

Corresponding author: Abhishek Bihani (abihani@utexas.edu)

Key Points:

- High silt content in mudrocks helps preserve large pore throats and lowers percolation threshold due to silt bridging.
- Silt bridging can create strong force chains between large grains and their neighbors on compaction upto a stress limit.
- Lower percolation threshold may allow trapped hydrocarbon or CO_2 to escape across the seal below fracture pressure.

Abstract

Mudrocks serve as geological seals for carbon sequestration or hydrocarbon formation where mudrock capillary seals having high capillary entry pressure prevent leakage of underlying fluids. However, seal failure can occur if the trapped nonwetting fluid escapes by porous flow or by induced tensile fractures caused by elevated nonwetting phase pressures. Since mudrocks are mainly composed of silt and clay size grains, a silt bridging effect has been observed when there are sufficiently abundant silt size grains. This effect creates force chains across the rock to help preserve large pores and throats and can reduce the sealing capacity of a mudrock. We used network models and discrete element (DEM) models to determine the conditions under which silt abundance will cause a mudrock seal to fail and allow a non-wetting fluid like CO2 or natural gas to flow. We show that when larger grains in a grain pack become 40-60 % of total grain volume, the drainage capillary pressure curves display two percolation thresholds, and the percolation threshold transitions to a lower value allowing seal failure even below tensile fracture pressure. The DEM compaction simulations found that strong force chains are mostly formed across grain contacts between large grains and their neighbors and not between small grains, which decreases coordination numbers and shields pore space from compaction before reaching a stress limit. Thus, through better understanding of grain concentrations and sizes on fluid flow behavior, we can improve risk management efforts in anthropogenic storage and estimates of reserve capacity of reservoirs.

Keywords: carbon sequestration, petroleum exploration, pore-scale modeling, mudrocks, capillary pressure, seal capacity

1. Introduction

Mudrocks act as good seals for sequestered human refuse such as radioactive waste or carbon dioxide, and for hydrocarbons. This is due to advantageous properties like high capillary entry pressure, low permeability, high sorption capacity, high ion exchange capacity and high swelling ability (Song and Zhang, 2012). However, while mudrock seals prevent the vertical movement of fluids and trap them in reservoirs over geological timescales, they can suffer failure and allow leakage under certain conditions. This may occur through three possible ways: Darcy flow, flow through faults and fractures, or diffusion (Ingram et al., 1997).

The porosity of sediments typically decreases with depth due to consolidation and cementation, which expels the fluids in the pore space and also reduces the size of the pores (Revil et al., 1999). The flow of a non-wetting fluid such as CO_2 or natural gas in a porous medium is dependent on a well-connected system of large pores. If the larger pores are destroyed due to compaction, then the capillary percolation threshold can be higher than the tensile fracture pressure, and the fluids will remain trapped below the seal until the fracture pressure is reached. Such a sealing mechanism is called a hydraulic seal (Watts, 1987). However, if the fraction of silt-size grains in a mudrock is sufficiently high, larger pores and throats may be preserved during burial. This will lower the percolation threshold and increase the possibility of fluid leakage through percolating pathways even below the fracture pressure. This occurrence has been termed in literature as quartz shielding (Krushin, 1997), compaction shielding (Dawson and Almon, 2002), pressure shadowing (Schieber, 2010), and silt bridging (Schneider et al., 2011). Minh et al. (2014) and de Frias Lopez et al. (2016) additionally found that vertically applied stress is distributed along force chains across a few grains while protecting rest of the interstitial space from compaction. Thus, this effect (henceforth called the silt bridging effect) can significantly affect the caprock properties and sealing capacity.

In this paper, we build on previous work (Bihani and Daigle, 2019a), in which we studied the correlated heterogeneity in mudrocks using pore scale modeling with various bidisperse grain pack combinations (packings made of two different size randomly distributed grains) without compaction. Our work concluded that, on increasing the fraction of silt-size grains (> 40%), the percolation length (length of first path of non-wetting fluid across the geometry) and tortuosity decreased, while permeability and pore throat sizes increased for unconsolidated bidisperse grain packs. Here, we expand our analysis to consider petrophysical properties like permeability and capillary pressure of grain packs formed with and without considering the effect of gravity and consolidation for varying grain sizes, shapes, and concentrations, and compare them with experimental results in literature. The evolution of strong and weak force chains and coordination numbers for different contact types in bidisperse grain packs under uniaxial stress is also analyzed using the results of discrete element method (DEM) simulations. Therefore, this paper combines the approaches of 3D DEM simulations and invasion percolation simulations, in an attempt to improve our understanding of the changes that occur in intergranular pore space during mudrock burial for various cases.

2. Background

2.1 Sealing capacity of mudrocks

The sealing capacity of a caprock can be examined by considering a non-wetting phase displacing the wetting phase initially present in the pore space. The Washburn equation (1) (Washburn, 1921) states that intrusion of non-wetting fluid in a capillary of radius (r) is possible only if capillary entry pressure (P_e) within the pore is exceeded:

$$P_e = \frac{2\sigma\, cos\theta}{r} = P_{nw} - P_w, \quad (1)$$

where σ is the interfacial tension between the wetting/non-wetting fluids, P_w and P_{nw} are pressures in the two fluids respectively, and θ is contact angle measured through the wetting fluid.

The capillary entry pressure and corresponding pore throat size exert a first-order control on the thickness of a fluid that may be sealed beneath a mudrock. As the seal overlying a reservoir is made up of much finer grains than the reservoir rock, the pores and throats in the seal are also much smaller, which means that the capillary entry pressure of the seal is much higher than that of the reservoir. This effectively blocks the buoyant fluid migrating upwards in a water-wet reservoir from invading a capillary seal (Ingram et al., 1997).

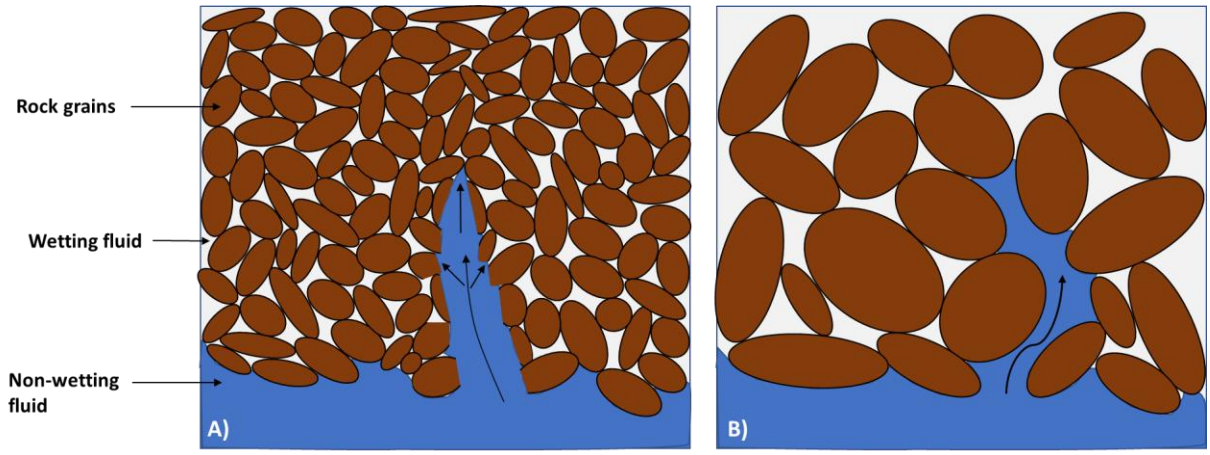

Figure 1- Influence of capillary pressure and grain size: A) fracturing, B) capillary invasion.

Jain and Juanes (2009) studied the relation between grain size and entry pressure and found a significant difference in behavior depending on the grain size of rock. In fine-grained rocks (Figure 1- A), the larger entry pressure favors mechanical effects and results in tensile fracturing or flow through existing fractures, since the capillary entry pressure may be greater than the sum of the minimum principal stress and the tensile strength (fracture pressure). A similar phenomenon can also occur because of dilation of rock fabric (Amann-Hildenbrand, et al., 2015). Conversely (Figure 1- B), for coarse-grained sediments having larger pores and

throats, the rock behaves as a rigid medium and capillary invasion likely occurs because the entry pressure is typically less the than fracture pressure. However, capillary entry does not necessarily lead to flow of the nonwetting phase across the medium. The breakthrough or threshold pressure (P_t) denotes the pressure at which a flow-path of non-wetting phase forms across the entire pore system and the percolation threshold is exceeded (Schowalter, 1979; Hildenbrand et al., 2002). Schlömer and Krooss (1997), and Hildenbrand et al. (2002) observed in their experiments that gas flow in mudrocks with multiple characteristic pore sizes occurred below the fracture pressure with mudrocks exhibiting dual porosity with bimodal pore sizes. Hence, mudrock seals with larger amounts of coarse grains are likely to leak by porous flow, while those having dominantly finer grains may suffer leakage through induced tensile fractures (Revil et al., 1999).

2.2 Force chains and silt bridging

Many studies have shown that the transport properties of mudrocks may be modeled by simplifying the porous medium as a bidisperse mixture of coarse (silt-size) and fine (clay-size) grains (Revil and Cathles, 1998; Schneider et al., 2011; Daigle and Reece, 2015; Daigle and Screaton, 2015; Daigle et al., 2015). The porosity of mixed grain size populations has been studied by those interested in packings of particles in artificially created mixtures and geological materials (Clarke, 1979; Allen, 1985; Marion et al., 1992; Koltermann and Gorelick, 1995). They found that the porosity of the mixtures differs according to the fractional concentrations of the different grain sizes and their radius ratio, and that the porosity of any binary mixture is less than the porosity of the individual components in the mixture In recent years, studies have also been conducted by a number of researchers in civil engineering (Sanchez-Arevalo, 2013; Minh et al., 2014; de Frias Lopez et al., 2016; Gong and Liu, 2017; Zhou et al., 2016; Wu et al., 2017; Deng

and Dave, 2017; Gong et al., 2019) using DEM, which is a particle-based numerical technique to solve for imposed forces. This has helped improve the understanding of stress-related changes that occur in intergranular pore space of heterogeneous grain mixtures used for construction. Therefore, applying such an approach to examine the structural, mechanical, and petrophysical behavior of bidisperse grain packs at different grain concentrations undergoing compaction can provide an insight into how the pore space in a mudrock evolves under overburden stress.

When a grain pack is subjected to an external loading, column-like structures for force transmission are formed due to the disordered packing (Majumdar and Behringer, 2005). These structures, called force chains, are formed across the neighboring grains in contact with each other, and can be differentiated into strong and weak force networks based on whether they are larger or smaller than the average force magnitude (Radjai and Roux, 1995). Radjai et al. (1998) found that the strong force network is preferentially oriented parallel to the axis of compression and is more anisotropic than the weak network, since the new contacts in the strong network are formed along the axis direction of shear and are lost in the direction perpendicular to it. Moreover, they found that the strong force chain network carries the majority of the external load and behaves like a solid with long range spatial correlations that tend to be larger than the grain size, while the weak network behaves like an interstitial liquid and does not carry major loads. Minh et al. (2014) and de Frias Lopez et al. (2016) studied the contribution of the different contact types like large-large (LL), small-large (SL) and small-small (SS) in the bidisperse grain packs under uniaxial compression and found that with increasing large grain concentrations, the force chain networks behave differently as amount of load carried by the larger grains also increases.

Similar behavior has also been observed in many petrographic studies of mudrocks where it is seen that the large, abundantly present silt grains redistribute the overburden stress across themselves and reduce the stress acting on the finer clay grains (Heling, 1970; Curtis et al. 1980; Oertel, 1983; Krushnin, 1997; Dawson and Almon, 2002; Yang & Aplin, 2007; Desbois et al., 2009; Day-Stirrat et al., 2010; Schieber, 2010; Day-Stirrat et al., 2011; Schneider et al., 2011 Pommer and Milliken, 2015). The bridging across neighboring large silt grains forms strong force chains which preserve the pores and throats in the interstitial space, and the sheltered pores and throats also remain large since the load bearing detrital grains reduce the alignment of clay grains present between them. Daigle and Reece (2015) found a trend of increasing permeability with decreasing clay concentrations in lattice-Boltzmann method (LBM) simulations of single-phase flow in high porosity systems. They found that mixture permeabilities can vary as per clay concentration and type, and the porosity of the mixture. Other experiments (Marion, 1990; Shakoor and Cook, 1990; Koltermann and Gorelick, 1995; Revil and Cathles, 1999; Guiltinan et al., 2018) also found that if the clay content decreases, the permeability and hydraulic conductivity of the silt-clay mixture increases. If silt bridging preserves a connected network of larger pores, the breakthrough pressure may be relatively small, thereby increasing the possibility of fluid leakage from the seal.

3. Materials and methods

We have used pore-scale simulations using DEM and network models to understand seal capacity in mudrocks and to determine the conditions under which a mudrock seal fails. The hypothesis we sought to test was that a mudrock seal can fail below the fracture pressure if there exists a percolating path formed due to a continuous large pore-throat system. This hypothesis was tested by simulating capillary drainage curves, permeability, force chains, and coordination

numbers from bidisperse packings of spheres. To study the percolation of a buoyant, non-wetting fluid across a caprock at varying grain concentrations, simulations were conducted with different large:small grain radius ratios, with and without considering gravity and compaction during the grain pack formation and burial. Figure 2 shows the different cases tested and the procedure followed during the modeling.

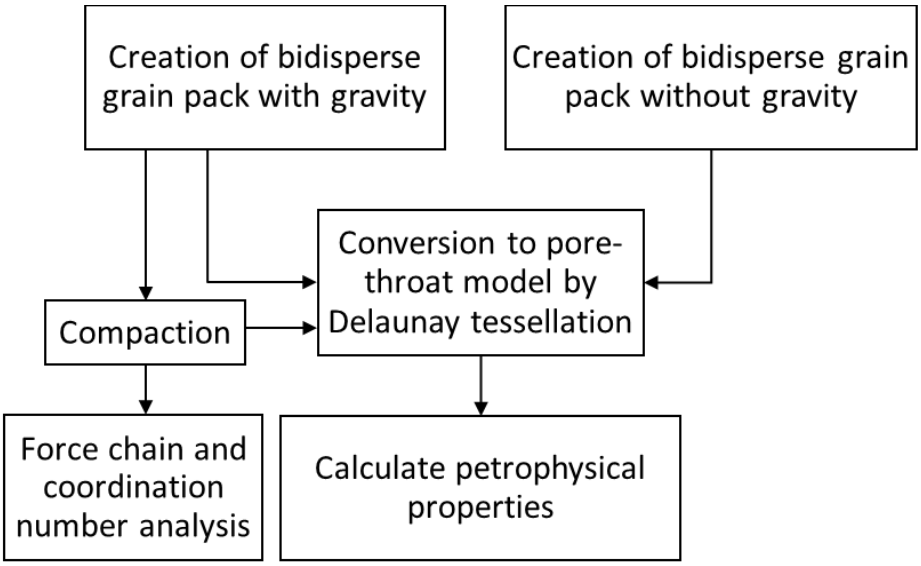

Figure 2- Cases and procedure in grain scale modeling

3.1 Bidisperse grain packing creation and compaction

To create a periodic, random system of bidisperse grains without gravity, a cooperative rearrangement algorithm was employed which varied the grain radii to get an efficient grain pack by minimizing porosity (Thane, 2006). We constructed grain packs with grain radius ratios (large to small) 5:1, 7:1, where the radius of smaller grains on average was ~0.1 units. Such ratios provided sufficiently sized grain packs with manageable computational times, representative of a mudrock seal consisting of a fine silt and clay mixture, e.g., silt-size grains ~10-14 μm and clay-size grains ~2 μm (Velde, 1996). The volume percentage of large spheres ($V_{\%L}$) can be found using equation (2):

$$V_{\%L} = \frac{100\, N_L {R_L}^3}{N_L {R_L}^3 + (N_T - N_L) {R_S}^3}, \quad (2)$$

where N_L is the number of large spheres, N_T is the total number of spheres, R_L is radius of larger spheres, and R_S is radius of smaller spheres. This variable was considered as the volume fraction of silt in the mudrock.

The grain packs were constructed considering gravity using two methods. Grain packs that were not compacted after creation were made with GeoDict software. The packs with bidisperse spherical grains were generated with radius ratios of 2:1, 5:1, 7:1, and 10:1 from 0 - 100 $V_{\%L}$ in additions of 10 $V_{\%L}$. Multiple grain packs were created for a particular $V_{\%L}$ and grain packs were also generated containing ellipsoidal clay grains to examine the difference in flow behavior. The ratio of the three axes of ellipsoidal grains was 3:2:1 with the major axis half the silt grain diameter.

The bidisperse grain packs considering the effect of gravity and compaction on the grains were created using LIGGGHTS, which is an open source discrete element method particle simulation software package, and stands for large-scale atomic/molecular massively parallel simulator (LAMMPS) improved for general granular and granular heat transfer simulations (Kloss et al., 2012). Similar to the workflow in GeoDict, grain packs were created in increments of 10 $V_{\%L}$ from 0 to 100 for a radius ratio of 7:1. This ratio was chosen for simulating compaction since it high enough to balance computational time while being representative of a mudrock. The grains were first inserted from the top in a cubic domain and allowed to settle under gravity. After the grains settled, an undrained constant rate-of-strain uniaxial consolidation test was simulated. First, the grain pack was confined between rigid walls laterally and from the bottom, while the top wall was kept as a movable servo wall. Then, the sample was compressed by moving the top wall vertically downwards and exerting a steadily increasing axial stress on the grain pack. The loading process consolidated the grain pack at a constant strain rate ($\dot{\varepsilon}$) of

about 0.2 s^{-1} until reaching a maximum axial stress of 2 MPa. The rigid lateral walls allowed the cross-sectional area of the grain pack to remain constant (zero lateral strain) throughout the simulation, while increasing only the axial strain. It was ensured that the process was quasi-static by keeping the inertial number ($I_n = 2 \times 10^{-9}$) less than 10^{-3} (Wu et al., 2017). I_n is defined as

$$I_n = \dot{\varepsilon}\sqrt{\frac{m}{Pd}}, \tag{3}$$

where m and d are the mass (4.2×10^{-15} kg) and diameter (2×10^{-5} m) of a small grain, and P is the applied stress (2 MPa). The behavior for three cases are highlighted during the test, A) Before compaction, B) Limited compaction (axial strain ~0.05), C) Final compaction (maximum axial strain > 0.2).

Figure 3A shows the variation of porosity (y-axis) with large grain concentration (x-axis) as the grain packs undergo compaction. The porosity values reduce as grain packs are compressed, but the reduction follows a consistent trend and the lowest porosity after compaction is for the same grain size concentration ($V_{\%L} = 60$) as observed before compaction. Figure 3B shows the porosity trends for bidisperse grain packs with different radius ratios with and without gravity, without compaction. It is seen that as large grain concentration increases, the porosity decreases to a minimum around 65-70 $V_{\%L}$ and then increases again as observed in experimental bidisperse packings. However, the porosity values are higher in the absence of compaction.

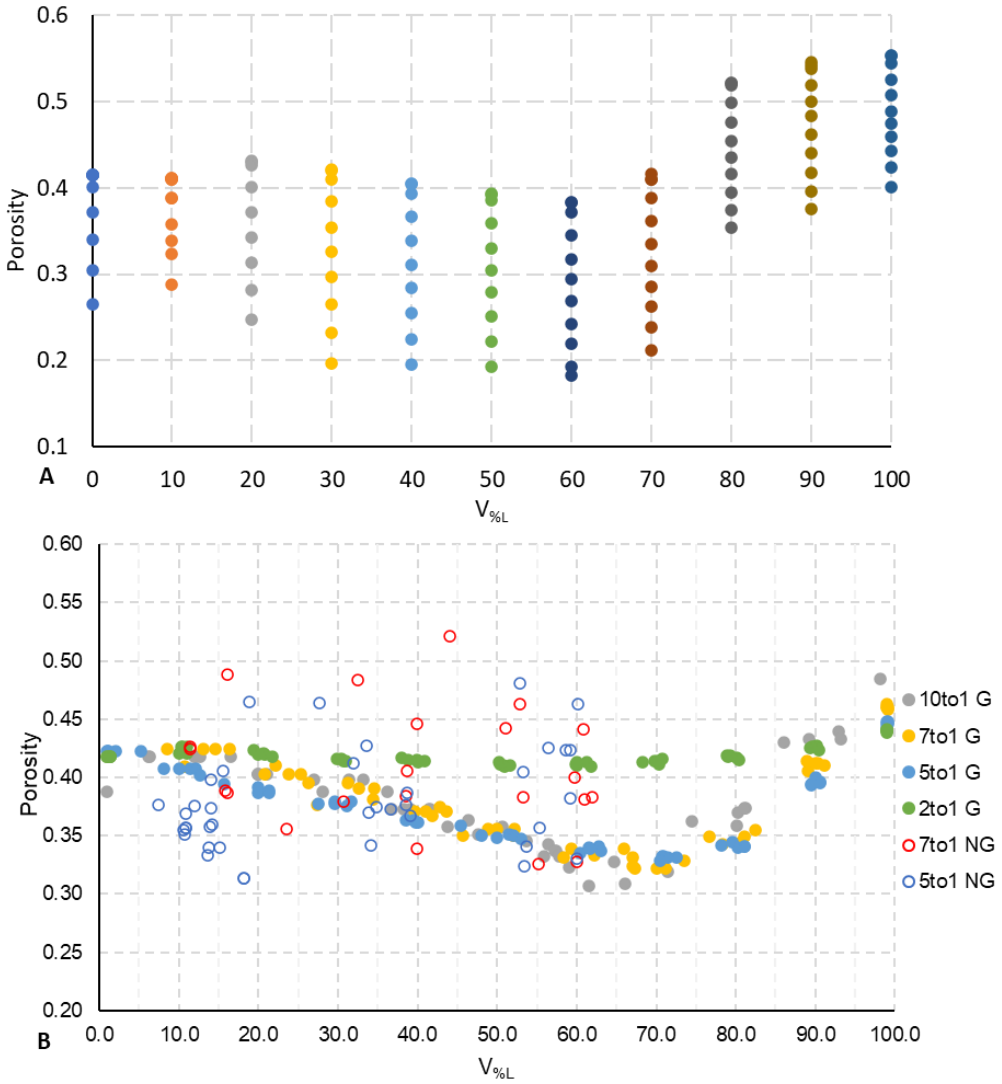

Figure 3- A) Porosity variation for 7:1G grain packs with compaction, B) Porosity variation for grain packs without compaction (G- Grain packs created with gravity, NG- Grain packs created without gravity), Modified after Bihani and Daigle (2019a).

In the literature, the minimum porosity of silt-clay mixtures was observed to occur at different values of clay content by weight: ~0.21 (Kolterman and Gorelick, 1995); ~0.4 (Shakoor and Cook, 1990); ~0.3 (Marion, 1990) and ~0.4 shale (clay) content by volume (Revil and Cathles, 1999). Grain packs whose radius ratios are smaller deviate more from the ideal porosity model. This happens as the voids between the coarser grains become smaller than the finer grains and increase the porosity. Even if the grain packs (with and without considering gravity) are not simulated under overburden pressures (Figure 3B), values of porosities generated (0.31 – 0.45)

are still comparable to sediments observed in consolidated marine clays (0.3 – 0.4) (Velde, 1996). Since the electrostatic repulsion effects and high specific surface areas of clays are not captured by the simulations, the initial porosity seen at lesser $V_{\%L}$ fractions in Figure 3A and B (~0.42), is lower than observed in experiments (~0.6) (Koltermann and Gorelick, 1995; Revil and Cathles, 1999).

3.2 Delaunay tessellation

Using the coordinates of the sphere centers and the radii of the spherical grains, the grain pack can be converted to a pore-throat model by Delaunay tessellation (Bryant et al., 1993). As seen in Figure 4, four spherical grains that are the nearest to others form a tetrahedral pore, and a cylinder called the throat connects any two neighboring pores across the face of the tetrahedral (Behseresht et al., 2009).

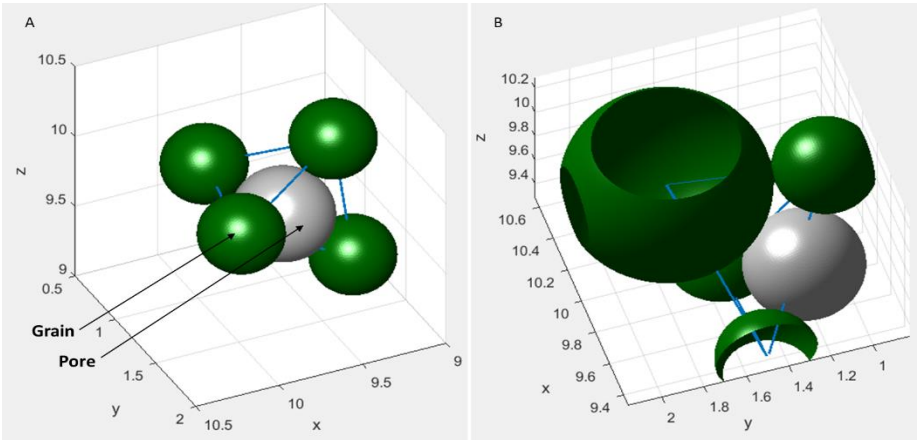

Figure 4- Example of Delaunay pore (grey): A) Between equal grains (green); B) Between unequal grains (green).

The conventional Delaunay tessellation method is known to give unrealistic pores when the grains forming the tetrahedra are unequal in size (Al-Roush et al., 2003). This was resolved by modifying the tessellation method to calculate the coordinates and radii of the pores when inscribed between differently sized grains. This constituted solving a matrix containing the radii of the four neighboring grains and distances between them as independent variables, and radius

of the inscribed pore as the unknown variable (Mackay, 1973). Additionally, the method was further modified to resolve complex cases where multiple tetrahedra formed overlapping pores which could lead to flattened tetrahedra with abnormally high radii (greater than the radius of the larger grain). Delaunay tessellation was employed to find the pore throat networks for all grain packs with spheres.

3.3 Capillary pressure and permeability calculations

The capillary pressure curve in the grain packs composed only of spherical grains (with and without compaction) was found by applying an invasion percolation algorithm to the obtained pore throat network. The Young-Laplace equation (4) describes the relationship between pressure to force a fluid in (or out) of a porous medium and the size of the pores (Mason and Mellor, 1995):

$$P_c = \sigma C = \sigma \left(\frac{1}{R_1} + \frac{1}{R_2}\right), \quad (4)$$

where P_c is capillary pressure, σ is interfacial tension, C is fluid meniscus curvature, and R_1, R_2 are principal radii of curvature. The fluid menisci at equilibrium are surfaces of constant curvature which form the interface between the fluids. The grains were assumed to be perfectly wetting with unit interfacial tension between the fluids. During drainage, the increasing system pressure was used to estimate the capillary pressure. At a certain system pressure, a non-wetting fluid entering from one side successively passes through the connected pore throats until the pressure cannot overcome a throat's entry pressure. Thereafter, the system pressure was raised, and the procedure was repeated until the invading fluid percolated to the opposing side. At every pressure step, the fluid saturation was calculated, which allowed construction of a capillary drainage curve. The absolute permeability of the grain packs composed of spherical grains was found by modeling the flow of one phase and allotting conductivities to pore throats (Bryant et

al., 1993). Since the Delaunay tessellation cannot create pore throat networks for grain packs containing ellipsoidal grains, after generating grain packs with ellipsoidal grains in GeoDict, absolute permeability and capillary pressure was calculated withing GeoDict (GeoDict User Guide, 2017). More details on the workflow are available in Bihani and Daigle (2019a).

3.4 Force chain and coordination number analysis with compaction

The results of the uniaxial test simulations (compacted grain packs) were post-processed to calculate the coordination numbers and study the force chain behavior for the different grain contact types across the bidisperse grain packs. For any particular grain in a pack, the coordination number (number of other grains in contact) is equal to the total number of force chains connected to the particular grain. These force chains can be divided into strong and weak networks, depending on whether they are larger (strong) or smaller (weak) when compared with the mean force magnitude. A stricter definition of differentiating strong and weak force chain networks has been used in some studies (Peters et al., 2005; Zhou et al., 2016; Deng and Dave, 2017) by also considering parameters like the number of consecutive chains and the angles between them, but it has not been implemented in our simulations as it does not account for cases where a force chain splits into two chains, and as the present definition gave satisfactory results.

Figure 5 shows the coordination numbers and strong and weak force chains in a grain pack with a high $V_{\%L}$. The total coordination number for a grain is the sum of the grain-to-grain contacts with all the neighboring large (orange) and small (green) grains, and is also the sum of the total strong (black) and weak (blue) force chains connected to that grain. For every step in the compaction process, the mean coordination number of the large grains in the pack was calculated for all the force chains as well as the strong chains. Similar calculations were conducted for the small grains in all the grain packs undergoing compaction. Among all the strong chains in a pack

for a particular compaction step, the fraction of large-large, small-large and small-small chains were calculated, and the evolution of their trend with respect to the axial strain was measured for the grain packs with varying large grain concentrations.

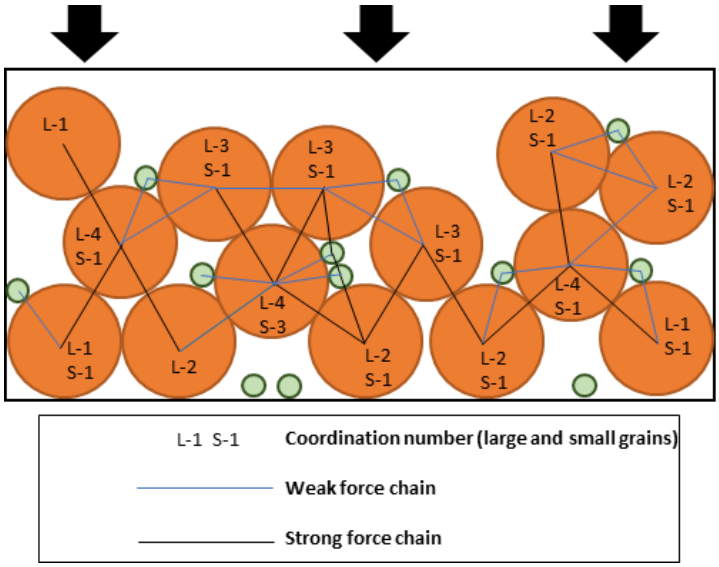

Figure 5- Coordination numbers (L- large orange grains, S- small green grains), weak (blue) and strong (black) force chain networks in a grain pack.

3.5 Comparison with experimental results

To compare the permeability and capillary pressure results from our simulations and the experiments in literature, the simulation results need to be converted to the appropriate units. The permeability (in Darcies) was calculated by assuming the silt grains from the simulations with a radius of 0.7 normalized units to be equivalent to a silt grain with radius of 4 μm. The capillary pressure was scaled to CO_2-brine system (MPa) from the unit interfacial tension and zero contact angle using the Washburn equation (1), assuming interfacial tension of CO_2-brine system equal to 0.03 N/m and keeping the wetting angle equal to zero degrees (Guiltinan et al., 2018). The entry pressure and the threshold pressure values were interpreted from the capillary pressure curve based on the first inflection point and the first percolation threshold observed and in some cases the entry pressure and threshold pressure were found to be the same. Thereafter, the

absolute permeability and capillary pressure results of our simulations were compared with those from Crawford et al. (2008) and Guiltinan et al. (2018).

4.0 Results

4.1 Representative elementary volume check

While representative elementary volume (REV) can be checked using variables like number of grains or pores, we designed a porosity-based method to check if the simulated grain pack sample was larger than the minimum volume required for accurate computation (Blunt, 2017). The porosities of subsamples of the control volume were calculated at various length scales in all three dimensions and then plotted. In Figure 6 A, we can see the REV plot of a cubic grain pack having 60 $V_{\%L}$ and 10:1 G ratio with length 4.7 units. When the subsample lengths approach the sample length, the porosities narrow towards a mean value (0.306), and the standard deviation decreases to zero (Figure 6 B). This shows that grain pack is greater than the required REV size.

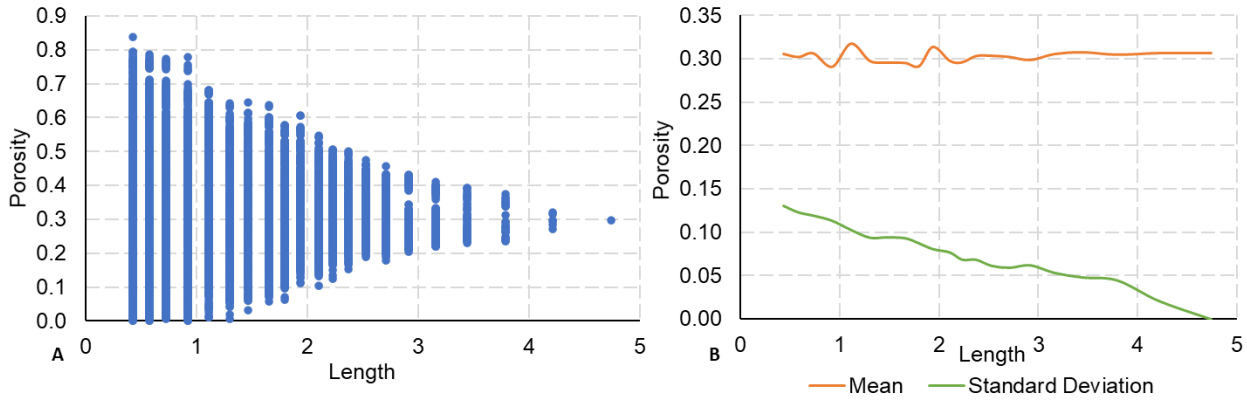

Figure 6- REV for 10:1 G grain pack: A) Porosity values; B) Standard deviation and mean.

4.2 Drainage capillary pressure

Figure 7 shows the drainage curves of grain packs with radius ratio 7:1 (with gravity and compaction) in increments of 10 $V_{\%L}$ having the wetting saturation on x-axis, and the capillary pressure on the y-axis. The capillary pressure values are dimensionless due to the assumption of

0° wetting angle on the grains and unit interfacial tension. The capillary pressure behavior before compaction (Figure 7A) shows two distinct thresholds (lower thresholds around 15-20, and higher thresholds around 60-70) and increasing the concentration of larger grains cause the transition from lower to higher threshold to be at successively smaller values of wetting fluid saturation. Similar behavior was seen in the curves for different radius ratios without compaction (Figure S1-S5 available in supporting information). The percolation thresholds increase on compaction, which is small for limited compaction thresholds (lower thresholds around 15-20, and higher thresholds around 65-75) in Figure 7B, but is more significant at end of compaction (lower thresholds around 18-25, and higher thresholds around 75-155) in Figure 7C. This is possibly since the size of pores and throats will decrease under increasing compaction, which increases the capillary pressure required for a non-wetting fluid to percolate across the medium.

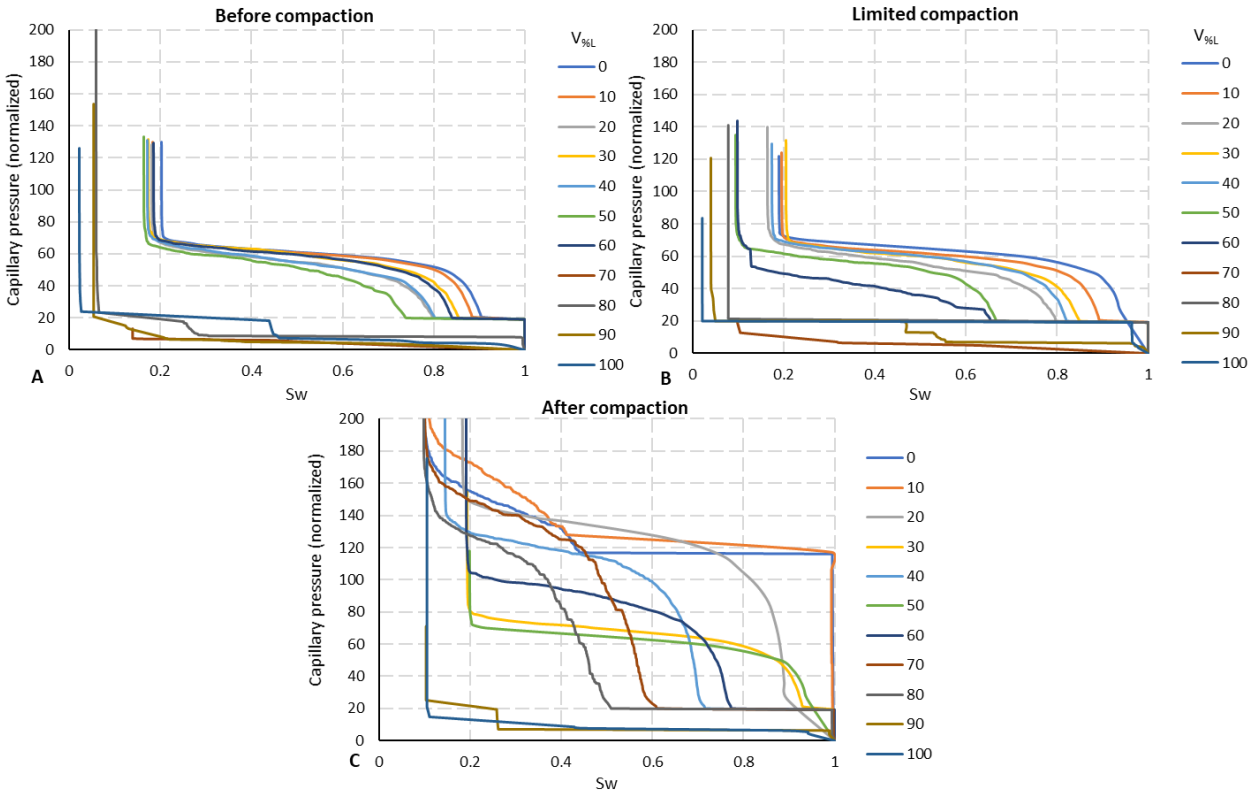

Figure 7- A, B, C - Drainage capillary pressure curves for different V%L (grain packs of ratio 7:1 G with compaction).

Figure 8 shows the behavior of grain packs with ellipsoidal grain packs for different grain concentrations without compaction. The porosity and permeability in Figure 8A show similar behavior as those with spherical clay grains. Permeability (normalized) successively increases with increasing fraction of silt grains, and porosity values first reduce and then increase. Figure 8B shows normalized capillary pressure curves for different values of $V_{\%L,}$ where percolation thresholds occur at progressively smaller values with increasing $V_{\%L}$ as in the spherical clay grain packs. The lower percolation threshold pressure (values 50 to 60) corresponds to larger radii (smaller curvatures) while the higher threshold (values 90 to 100) corresponds to smaller radii (larger curvatures).

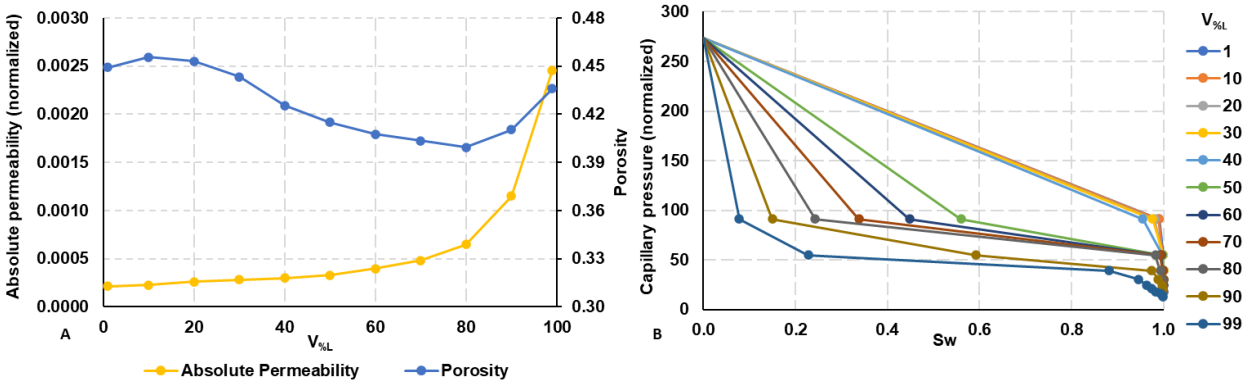

Figure 8- Results for ellipsoidal grain packs: A) Porosity and permeability, B) Drainage capillary pressure curves.

As during the capillary pressure curve generation for all grain packs, the pressure was controlled and not the fluid saturation, and as the capillary pressure curves generated were relatively flat, each curve had a small number of different saturation values. Hence, as the generated relative permeability curves too had fewer data points and did not offer any significant addition to the results, they are not included.

4.3 Absolute permeability

As the absolute permeability of a rock depends on the geometry of its connected pore network and the direction, the vertical absolute permeability for the sphere-packs was simulated

and is shown in Figure 9A, and the values are normalized by square of the domain length. As the large grain concentration is increased, the permeability increase is not significant for lower values (< 35 $V_{\%L}$). However, the permeability values for grain packs of all radius ratios increase steadily from 35 $V_{\%L}$ until 70 $V_{\%L}$, after which the values remain constant. The permeability values for grain packs without gravity (NG) are higher than the corresponding grain ratio grain packs with gravity (G) with more scatter, possibly due to the less dense and more random packing of grains. Figure 9B shows the absolute permeability for 7:1 G grain packs with compaction. The absolute permeability values decrease with compaction, since the values at end of compaction are lower than those at limited compaction, which are lower than those before beginning compaction.

Figure 9C shows the cross-plot of absolute porosity and permeability for 10:1 G grain packs from 10 to 70 $V_{\%L}$. Despite some scatter seen due to grain pack heterogeneity, in general, the absolute permeability increases with decreasing porosity. This occurs because with increasing large grain concentration, the porosity initially decreases (Figure 3), and the absolute permeability increases (Figure 9A). Also, there are two trends seen in the plot. For a single porosity, the permeability increases as the proportion of silt grains increases, likely because of the preserved larger pore throats. Secondly, as porosity decreases, the permeability only remains constant if the concentration of large grain increases. This indicates there is a competing effect between the permeability reducing following a decrease in porosity, and the effect of more large grain concentrations causing an increase in the permeability.

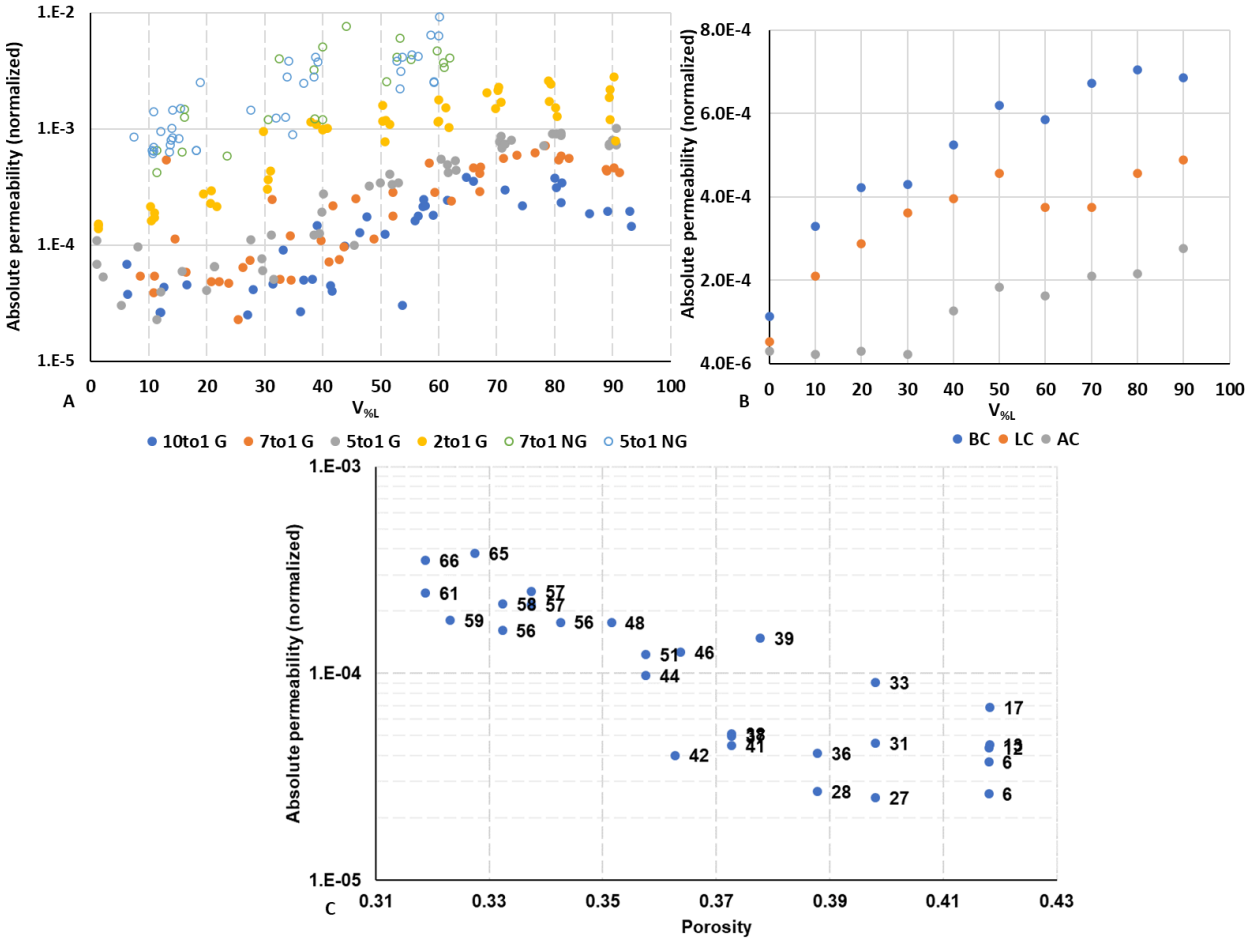

Figure 9- A) Absolute permeability of the simulated grain packs without compaction (G- Grain packs created with gravity, NG- Grain packs created without gravity), B) Absolute permeability of 7:1 G grain packs with compaction, C) Cross-plot of porosity and absolute permeability for 10:1 G grain packs from 10-70 V%L with data labels of V%L.

4.4 Capillary pressure and permeability comparison with experiments

The absolute permeability (in Darcy) of the grain packs without compaction for the radius ratios 10:1, 7:1, 5:1 G and grain packs with ellipsoidal clay grains are shown in Figure 10A, and for radius ratios 7:1 G for different compactions are shown in Figure 10D. These simulation results are compared with the experimental results of Crawford et al. (2008) and Guiltinan et al. (2018) as a function of the silt concentration. The trends from both, simulations and experiments in Figure 10A and D seem to be similar with absolute permeability increasing with silt concentration. In both figures at lower silt concentrations, the simulated permeability values are observed to be higher than the experiments but become similar at larger silt fractions

409 (~75 $V_{\%L}$). In Figure 10D, the permeability values before compaction and for limited compaction
410 are high (>10^{-4} D), while they are observed to decrease by the end of compaction, especially for
411 $V_{\%L}$ < 40.

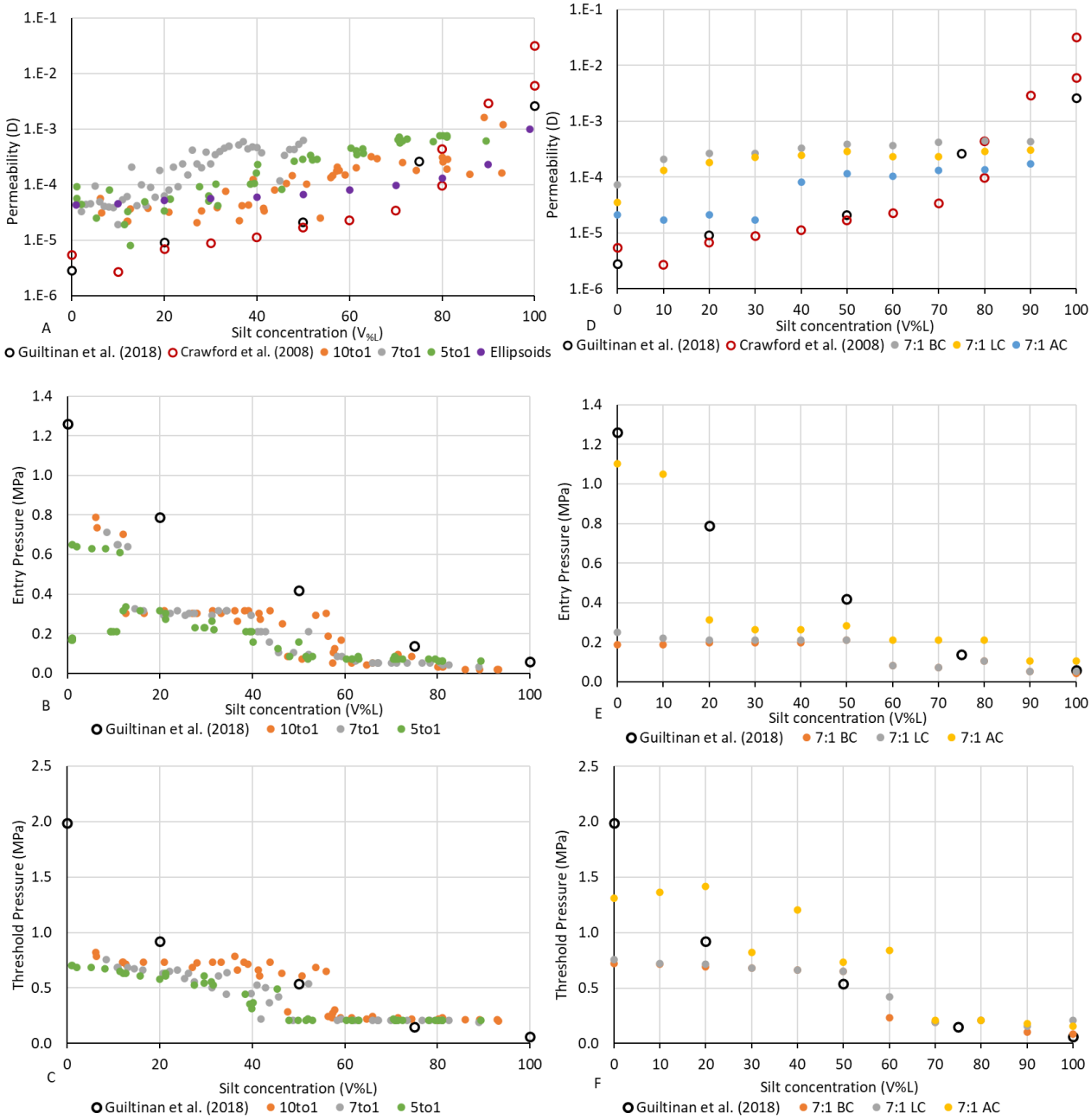

412

413 **Figure 10**- Comparison of simulation and experimental results: A) absolute permeability (no
414 compaction), B) Entry pressure (no compaction), C) Threshold pressure (no compaction), D)
415 absolute permeability (compaction), E) Entry pressure (compaction), F) Threshold pressure
416 (compaction). (BC- Before compaction; LC- Limited compaction; AC- After compaction).

The entry pressure and the threshold pressure of the grain packs without compaction (Figure 10B and C) and with compaction (Figure 10E and F) are compared with the experimental results of Guiltinan et al. (2018) as a function of the silt concentration. Both the simulations and experiments follow the general trend of higher values at low silt concentrations which decrease with increasing silt fraction. However, the simulated values are not as high as those observed in experiments, especially at low silt concentrations (< 20 $V_{\%L}$). In Figure 10B, the simulation entry pressure values are about 0.6 - 0.8 MPa at $V_{\%L}$ < 15 but decrease to 0.2 - 0.3 MPa for $V_{\%L}$ > 15%, and further decrease to < 0.1 MPa for $V_{\%L}$ > 50. While the entry pressure values in Figure 10E follow a similar trend, the entry pressure for $V_{\%L}$ < 20 after compaction is comparable to the experimental values (> 1 MPa). In Figure 10C, the simulation threshold pressure values are 0.6 - 0.8 MPa for $V_{\%L}$ < 50% and decrease to ~0.2 MPa for $V_{\%L}$ > 50. In Figure 10F, the threshold pressure trend for cases before compaction or at limited compaction is similar to Figure 10C, where values become < 0.5 MPa for $V_{\%L}$ > 50. However, the threshold pressures are larger than the experimental values at for grain packs at end of compaction for 10 < $V_{\%L}$ < 70.

4.5 Force chain and coordination number analysis during compaction

Figure 11A, B, C, D shows the mean coordination numbers of 7:1 G grain packs as a function of axial strain during compaction. Figure 11A shows the mean coordination number of large grains for all force chains (LG, AFC), Figure 11B shows the mean coordination number of small grains for all force chains (SG, AFC), Figure 11C shows the mean coordination number of large grains for strong force chains (LG, SFC), and Figure 11D shows the mean coordination number of small grains for strong force chains (SG, SFC). For each plot, observations about coordination number can be made for increasing axial strain and for increasing $V_{\%L}$.

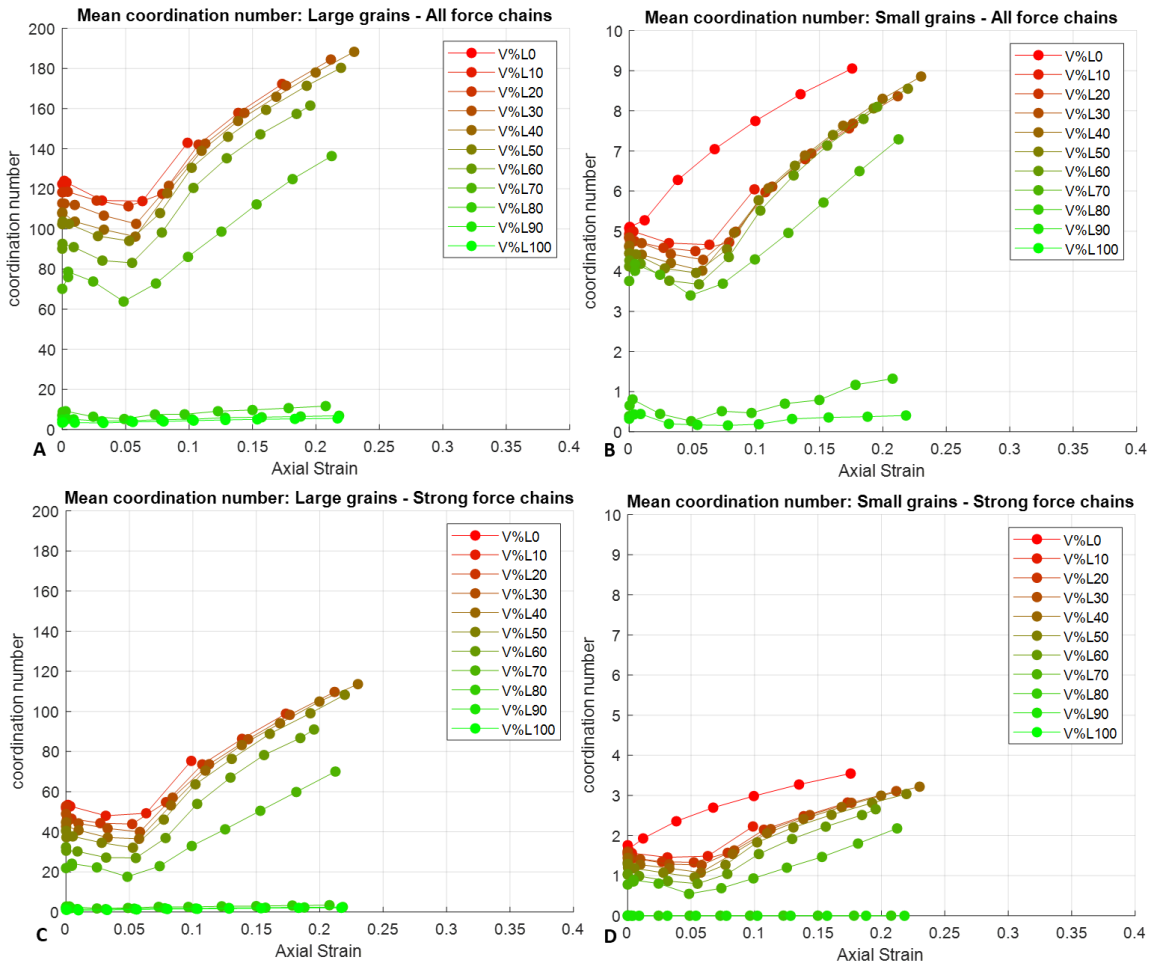

Figure 11- Mean coordination numbers of grain packs as a function of axial strain. A) large grains for all force chains, B) Small grains for all force chains, C) Large grains for strong force chains, D) Small grains for strong force chains.

In Figure 11A, with increasing axial strain, the mean coordination number- large grains, all force chains, for grain packs with $V_{\%L}$ from 10 to 70 first decreases from a range of 75 - 122 to a range of 60 - 115 when the axial strain reaches a value of ~0.05, and then begins increases again for the later stages of compaction to a final range of 138 - 190. At one fixed strain, with increasing concentration of large grains, the mean coordination number decreases, possibly due to fewer number of small grains being available for close contact with the larger grains. For grain packs greater than 70 $V_{\%L}$, the behavior is noticeably different with much smaller values (4 - 15), as the grain pack matrix is made up of large grains with a very small population of small grains

existing in the interstitial space, whereas before 70 $V_{\%L}$, the mean coordination number is high as a large number of small grains are in contact with every large grain in the pack and the matrix is made up of small grains.

In Figure 11B, C, and D the behavior for mean coordination numbers as a function of axial strain is somewhat similar to Figure 11A, whereby with increasing strain, the values initially decrease before increasing again, and for a single strain, the values decrease with increasing large grain concentration. However, in Figure 11B, the values of coordination numbers are smaller as the small grains are only in contact with few other grains compared to the large number of small grains one large grain can contact. In Figure 11C, the values of coordination numbers are smaller than those in Figure 11A, as only the strong chains are considered for the calculations. Similarly, in Figure 11D, the values of coordination numbers are smaller than those in Figure 11B, as only the strong chains are considered for the calculations.

Figure 12A, B, C shows the fraction of strong force chains and D shows the contact type contributions in 7:1 G grain packs as a function of axial strain during compaction. For each plot in Figure 12, observations can be made for increasing axial strain and for increasing $V_{\%L}$. Figure 12A shows the fraction of strong chains connected across large-large grains as a function of axial strain. For $V_{\%L}$ values greater than 70%, almost all the strong chains are across the large-large grains as the large grains form the matrix. For $V_{\%L} < 70$, the large-large fractions of strong chains are a small portion of the total strong chains, as very few large grains are in contact with each other and with decreasing large grain concentrations, the values successively decrease further. It is also seen that for grain concentrations of $40 < V_{\%L} < 70$, as strain increases, there is a slight increase in the values until reaching an axial strain of ~0.05, before decreasing again. Figure 12B shows the fraction of strong chains connected across small-large grains as a function of axial

strain. While for $V_{\%L}$ concentrations < 20 and > 80, the fraction of strong chains is lower than 0.05, the small-large fraction of strong chains increases as the $V_{\%L}$ concentrations increases steadily from 20 to 70. Moreover, the fraction values for grain concentrations of $40 < V_{\%L} < 70$, increase with increasing axial strain before becoming constant. Figure 12C shows the fraction of strong chains connected across small-small grains as a function of axial strain. At lower $V_{\%L}$, the fraction is close to 1 and decreases steadily with increasing large grain concentrations until reaching 70 $V_{\%L}$. The small-small fraction of strong chains at $V_{\%L} > 70$ is on the order of 10^{-3} and is not seen in the plot. The fraction values for grain packs with grain concentrations of $40 < V_{\%L} < 70$, decrease as the axial strain increases until ~0.05 and thereafter, become constant.

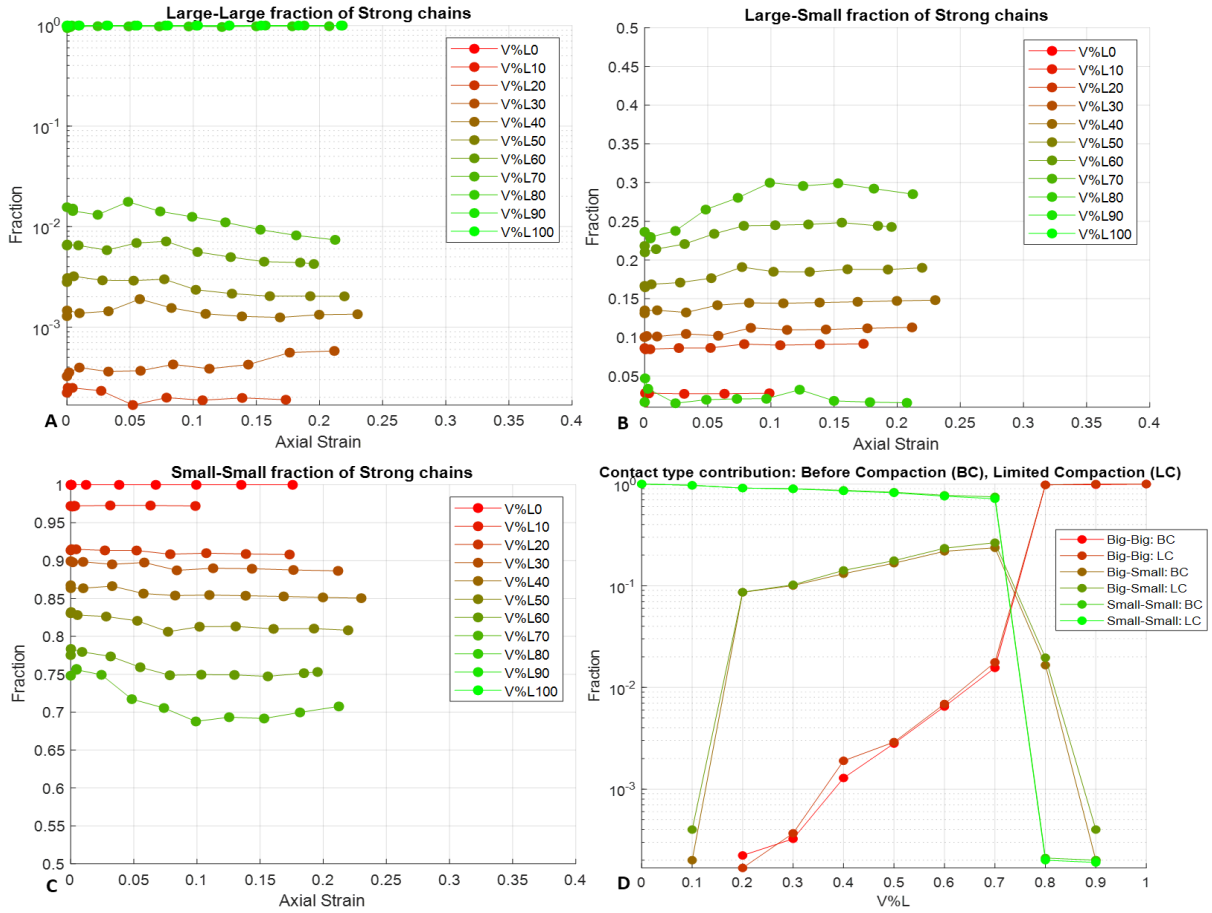

Figure 12- A) Fraction of strong chains connected across large-large grains, B) Fraction of strong chains connected across small-large grains, C) Fraction of strong chains connected across small-small grains, D) Contact type contribution as function of large grain concentration.

Building on the observations from Figures 12A, B, C, the Figure 12D shows the comparison of the large-large, small-large, and small-small fraction of strong chains before compaction and for limited compaction (axial strain = 0.05). For both cases, as fraction of large grains increases, contribution of small-small chains to the strong chains steadily decreases, the contribution of large-large chains to the strong chains steadily increases, and the contribution of small-large chains to the strong chains increases to a maximum value at 70 V%L and then decreases. Moreover, there is a slight increase in the small-large and large-large fractions at a particular $V_{\%L}$, when a grain pack is subjected to limited compaction.

5.0 Discussion

Figure 13 shows a 2D schematic of a grain pack, where the gravity on the grains acts vertically downwards. Because of silt bridging, the large pore throats may be sheltered between a system of large grains as fraction of larger grains increases (Schneider et al., 2011). This can happen even when the matrix of the grain pack is made up of smaller grains since the grains who are part of the strong force chains transfer the vertical stress on grains below them and shield the laterally present grains, thus creating a bimodal pore and throat distribution. This is further helped by the larger grains distorting the small grain network near their surfaces and creating larger voids.

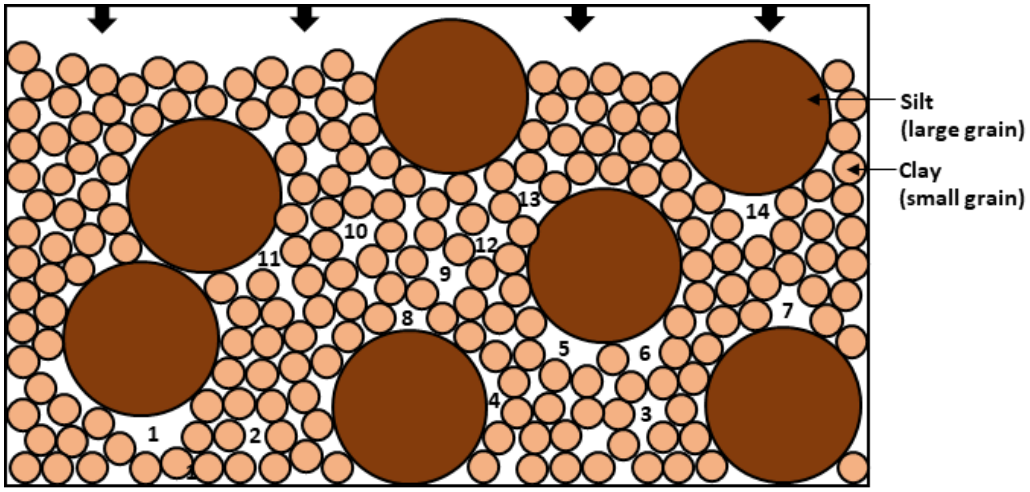

Figure 13- 2D Silt bridging schematic. Few large pores and throats are numbered.

5.1 Capillary pressure

Observing the threshold capillary pressure values in Figures 7 and 10 suggests that the percolation threshold is higher for low $V_{\%L}$, since the smaller pore-throat network does not allow the non-wetting fluid to flow through the grain pack. However, once large grains are abundant enough to preserve larger pore-throat networks (40 - 60 $V_{\%L}$), the non-wetting fluid can percolate, and the percolation threshold is lowered. This behavior is dependent on the silt bridging effect until the minimum porosity where the grain pack matrix transitions to the larger grains, resulting in the smaller percolation threshold completely controlling non-wetting phase transport. In Figure 7, as the grain packs get compacted the pores and throats start becoming smaller. For lower axial strains (≤ 0.05), the strong force chains formed across the larger grains shelters the pores and throats from compaction, which allows the percolation thresholds to stay close to the values before compaction. However, beyond a stress limit, the force chains cannot bear the stress, and the preserved pore space gets destroyed which increases the percolation threshold. Capillary pressure curves for ellipsoidal clay grain packs in Figure 8B show a trend similar to the grain packs with bidisperse spheres, with progressively lower percolation thresholds seen at higher silt grain concentrations (>40 $V_{\%L}$). As the elliptical grains are flatter

and smaller than the spherical grains, they fit better between the spherical grains and lead to higher capillary pressures even at high wetting saturations. However, the transition between the threshold values was observed to be more gradual rather than sharp, as the ellipsoidal grains may have caused a wider distribution of pore-throat radii values.

Torskaya (2013) investigated capillary pressure behavior using alternating layers of large and small spherical grains of radius ratio 3:1 and multiple cases of varying grain fractions. For vertical flow, only a single, high percolation threshold was observed due to the small pore-throats encountered for all flow-paths in the fine-grained layer. However, the capillary pressure behavior for horizontal flow was similar to our results with two percolation thresholds. As the grains and the corresponding pore-throat sizes offered competing pathways for the fluid, initially the layer of larger grains was invaded followed by invasion in the fine-grained one, resulting in two percolation thresholds. This behavior is analogous to our results where the dispersed grains of two sizes create a dual porosity system, and the fraction of larger pore-throats depends on the fraction of larger grains observed in the system. In their resedimentation experiments, Guiltinan et al. (2018) found that increasing the pore space between smaller grains affects the breakthrough pressure and permeability, even though the larger grains affect the mudrock structure. This is consistent with why higher pressures (> 0.6 MPa) are observed at lower $V_{\%L}$ in Figure 10B and C. Moreover, in Figure 10E and F, the entry pressure and threshold pressure values are even higher (> 1 MPa) for grain packs with low silt concentrations (< 30 $V_{\%L}$) at end of compaction, due to decrease in the void space between the finer grains.

5.2 Absolute permeability

Our simulations investigated the dependence of permeability on factors like volume fraction of clay and the associated porosity, the total porosity, grain size and shape, the packing

and compaction, and compared them with previously published results in literature. In Figure 9A and 10A, when the large grain fraction is below 35 $V_{\%L}$, the absolute permeability is low as the clay grains create impediments for flow through the pore throat network (Revil and Cathles, 1999). The gradually increasing absolute permeability after 35 $V_{\%L}$, is similar to the results seen by Daigle and Reece (2015) in their simulations for dilute systems, and in mixture experiments by Marion (1990), Shakoor and Cook (1990), Schneider et al. (2011), Crawford et al. (2008), and Guiltinan et al. (2018) which could be possibly attributed to silt bridging. At 70 $V_{\%L}$, when minimum porosity is reached, the matrix transitions to coarser grains as finer grains are no longer sufficient enough to form a continuous network. However, the finer grains fit in the voids between the larger grains and reduce the volume available for flow. This may be a reason why permeability remains constant by opposing the effect of silt bridging. For the cases of grain packs without gravity, the absolute permeability values are higher than the corresponding grain ratio grain packs with gravity. This could be due to the less dense grain packs formed by the cooperative rearrangement method, resulting in an early onset of the silt bridging effect.

The competing effect of reducing porosity and increasing large grain concentration on permeability is better seen in Figure 9C. As the large grain concentration in a grain pack increases, the porosity reduces as expected in a bidisperse packing, which has a negative effect on the permeability. However, with increasing large grain concentrations, the obstructions to fluid flow are reduced due to the large pores and throats and leads to an increase in the absolute permeability. This behavior was also observed for the grain packs with ellipsoidal grains where clay grains were less aligned at higher large grain concentrations (Figure 8A). Moreover, in Figure 9C, there are some instances where at a single porosity, there is a significant difference in permeability for different concentrations of larger grains. This behavior is similar to what was

seen by Schneider et al. (2011), where for Boston Blue clay and silt mixtures, the vertical permeability differed by an order of magnitude for the same porosity at different clay concentrations. They observed that for their 57% clay sample, the permeability was lowest, as the clay particles were well-aligned and the pores were small, while in their 36% clay sample, the pores were larger and concentrated around silt-size grains with less alignment of clay grains. Yang and Aplin (2010) used data from 303 mudrock samples with varying range of clay content (12-97%), to examine the porosity-permeability relationship. They also observed that the variability in the relationship is mainly controlled by the clay content, with a higher permeability at the same porosity for a lower clay content.

For the cases of grain packs undergoing compaction, in Figure 9B and 10B, the permeability values for limited compaction are slightly lower than those before compaction but reduce more significantly by the end of compaction, especially for $40 < V_{\%L}$ which have fewer silt grains to form force chains and shelter pores and throats. For the experimental results showed for comparison in Figure 10, the resedimentation slurry used by Crawford et al. (2008) and Guiltinan et al. (2018) consisted of quartz and kaolinite at different volume fractions which has undergone consolidation and cementation. However, the simulated grain packs shown in Figure 10 do not undergo any cementation, even if some grain packs are compacted. The grain packs are also bimodal in nature with grains of fixed sizes and shapes (spheres or ellipsoids). As a result, the void space in the grain packs may be greater than the slurry used in experiments, especially at smaller silt concentrations. This can cause a deviation between simulation and experimental results where the simulated permeability is greater (Figure 10A, D), and the simulated capillary entry pressures (Figure 10B, E) and threshold pressures (Figure 10C, F) are smaller than the experimental values. At larger silt concentrations, the experimental and simulation values may be

591 closer to each other possibly due to more load-bearing silt grains in the slurry leading to
592 increased pore-throat sizes, similar to the grain packs in the simulations.

593 **5.3 Force chain and coordination number analysis**

594 **5.3.1 Effect of grain pack compaction**

595 Figure 14-1, 2, 3 shows an example of three cases for a 60 $V_{\%L}$ grain pack subjected to
596 uniaxial testing, (14-1) Before compaction, (14-2) Limited compaction (axial strain ~0.05), (14-
597 3) Final compaction with a) 3D structure, b) 2D cross-section, and c) force chains shown for
598 each case. Figure 14-4 shows a 2D schematic of the evolution of the pore space in the grain pack
599 for the three compaction cases to better understand the behavior.

600 Before compaction (Figure 14-4a), the grains are in a less stable configuration with the
601 coordination numbers between the small and larger grains (SL) being less than the maximum
602 possible value (similar to Figure 14-1a, 1b). As seen in the example force chain diagram in
603 Figure 14-1c, the force chains before compaction all have mostly similar values with some lower
604 force chains having a relatively higher value (red) because of the weight of the grains over them.
605 Due to the high number of smaller grains in the pack, the majority of the strong chains are
606 formed between small-small grains, with an intermediate fraction of small-large chains, and a
607 very low fraction of large-large chains in the strong chain fraction.

608 In the limited compaction case (axial strain = 0.05), the larger grains in the 3D structure
609 (Figure 14-2a), no longer protrude from the top due to the force imposed by the top wall moving
610 downwards. As seen in Figure 14-4a, the grain packs undergo compaction and the grains try to
611 find a more stable configuration with grains (especially larger ones) moving closer to each other
612 (similar to Figure 14-2a, 2b). As the stress gets transferred downwards across the force chains,
613 the grains which are a part of the strong chains form linear chain-like structures in the vertical

direction (Deng and Dave, 2017). As seen in the strong chains (red) in Figure 14-2c, the transfer of vertical stress from the large grains to the grains below them (large or small), can shelter the smaller grains laterally present beside them from the vertical stress, and increase the large-large and small-large fraction of strong chains (Figure 12A, B), at the cost of the small-small chain fraction (Figure 12C). The compression can also push out the smaller grains lodged between the larger grains, leading to more large-large force chains formed between two larger grains in contact. Since there is an increase in the fraction of large grains which bear the vertical stress, it allows the grains in the weak network to settle stress-free, thereby preserving large interstitial pores (silt bridging). The grain realignment which creates linear structures across the grains is called jamming (Majumdar and Behringer, 2005), and can reduce the total number of contacts (coordination number) between the grains. It may occur as the jammed smaller grains in force chains lose lateral contact with the surrounding grains. This is observed during the transition from Figure 14-4a to b, and in Figure 11, where the mean coordination numbers in all the plots initially decrease before reaching an axial strain of ~0.05. Moreover, on comparing Figure 11A and C, or Figure 11B and D, it seen that the mean coordination number in strong chains is always lower than the mean coordination number in all force chains and may be an indication of the larger pore space formed in the grain surroundings. Tordesillas (2007) and Zhou et al. (2016) inferred that decreasing coordination numbers after compression of grain packs could be due to self-organization of the granular mixtures, where intergranular contact loss occurs in some grains due to axial loading. This behavior continues until a peak stress (limited compaction), where a minimum coordination number is reached, and the self-regulating contact network can no longer take any more external stress. Wu et al. (2017) conducted DEM compaction simulations of binary mixtures of radius ratio 2.5 and observed a decrease in the coordination numbers during

637 compaction up to a certain limit. They also observed that the coordination numbers for large and
638 small grains decreased as the proportion of large grains increased, due to underfilling of small
639 grains in the interstitial space between large grains.

640 On further axial compaction (Figure 14-4c), the force chains that have been formed
641 across grain contacts are no longer sufficient to bear the load and force chain failure may occur
642 through buckling or frictional slip, which unjams the grains (Tordesillas and Muthuswamy,
643 2009). Such force chain failures can be due to mobilization of the grain contacts by rolling or
644 sliding (Tordesillas, 2007), which will shift the grains out of the strong force chains and allow
645 the axial compression to cause loss of the pore space. Hence, after sustained compaction, the
646 small grains are highly compressed and occupy all the available space (similar to Figure 14-3a,
647 3b). This leads to an increase in the number of grain contacts for any small or large grain, leading
648 to increased mean coordination numbers. This behavior can be observed in transition from
649 Figure 14-4b to c, and in Figure 11 for all the plots. While the unjamming due to compaction
650 may reduce number of contacts between two large grains, and a decrease in large-large fraction
651 of strong chains (Figure 12A), the vertical stress is still transferred from the larger grains to the
652 grains below them. The large number of small grains surrounding one large grain (cf. Figure 14-
653 3c) will increase the number of small-large type strong force chains (Figure 12B), while
654 decreasing the small-small chain fractions (Figure 12C).

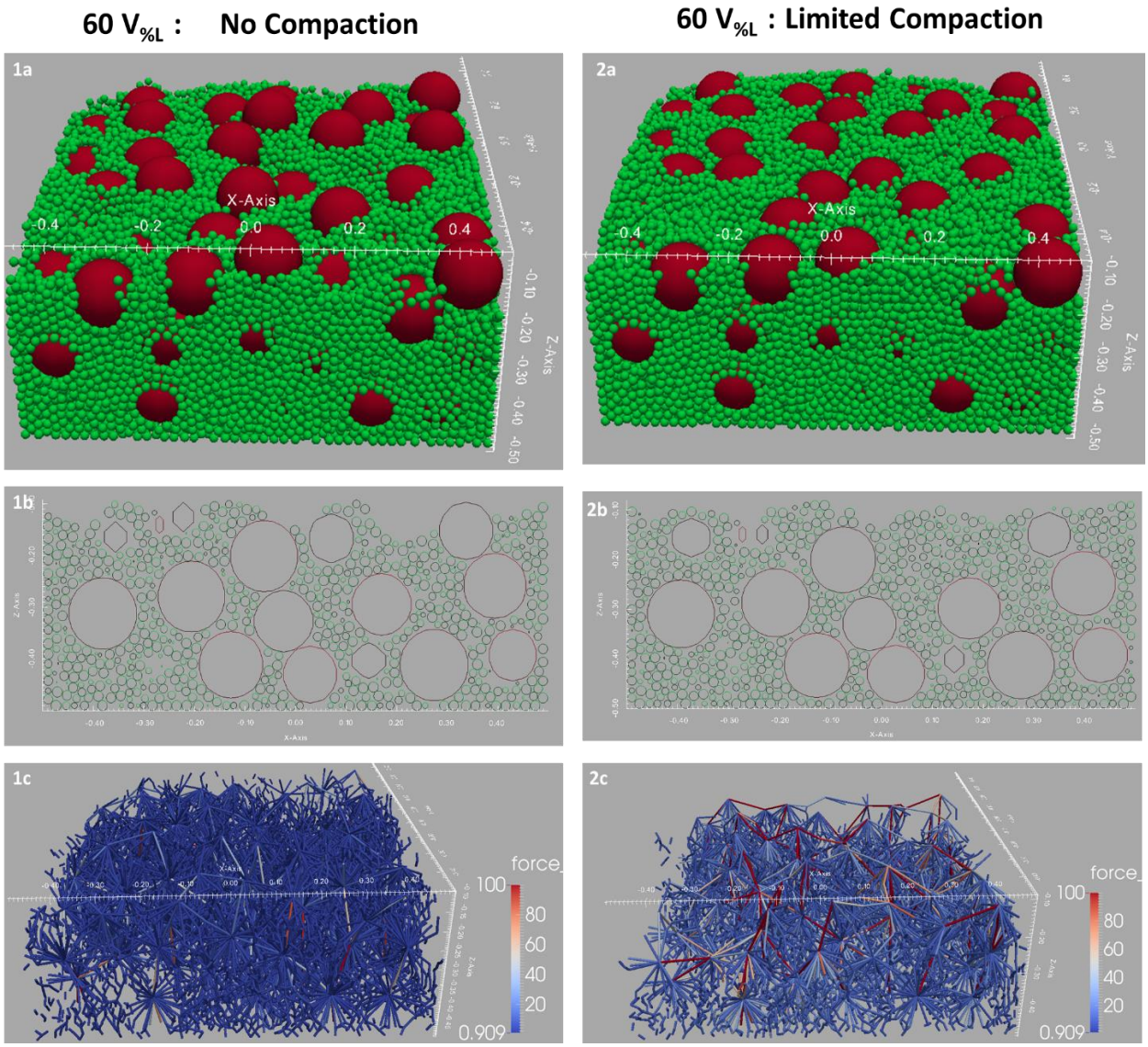

Figure 14- 60 V%L grain pack subjected to uniaxial testing- 1a) 3D structure before compaction, 1b) 2D cross-section before compaction, 1c) force chains before compaction, 2a) 3D structure on limited compaction, 2b) 2D cross-section on limited compaction, 2c) force chains on limited compaction.

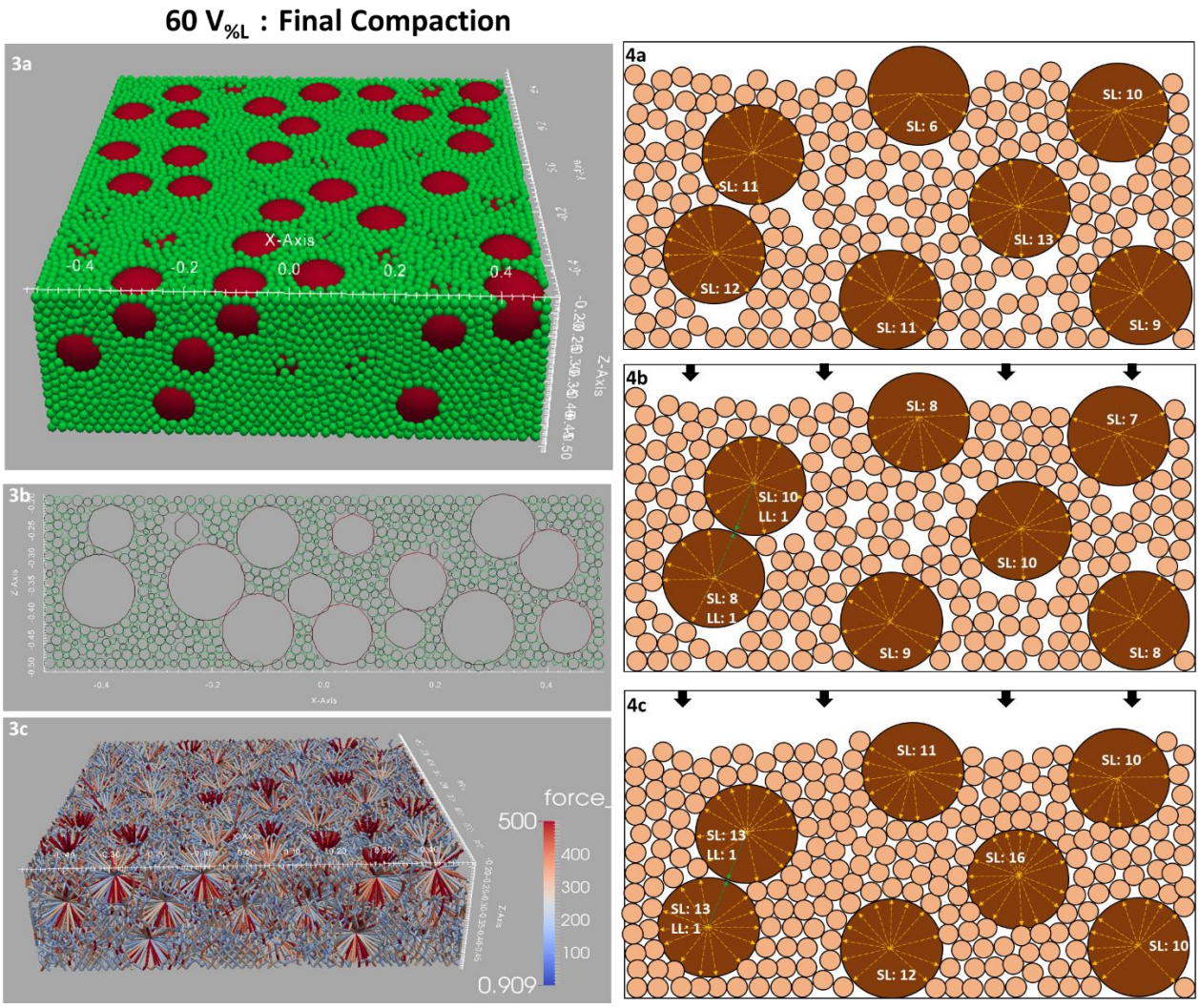

Figure 14 (continued)- 60 V%L grain pack subjected to uniaxial testing- 3a) 3D structure at final compaction, 3b) 2D cross-section at final compaction, 3c) force chains at final compaction, 4a) 2D schematic of grain pack before compaction, 4b) 2D schematic of grain pack on limited compaction, 4c) 2D schematic of grain pack at final compaction. (SL- small-large grain contacts, LL- large-large grain contacts).

5.3.2 Effect of increasing V%L in grain packs

Zhou et al. (2016) studied the effect of varying the radius ratio of binary mixtures during the DEM compression experiments and found that for larger radius ratios, there are many small grains with low coordination numbers due to the larger pore space between the larger grains preventing the smaller grains from contacting all the grains around them, thereby protecting them from the external stress. They also found that as radius ratio increases, the importance of large-large contacts in strong force chains also increases. This is because for size ratios > 4.4, the small

673 grain is too large to fit in the void space between four large spheres, so the large grains lose
674 contact with each other. Conversely, for cases like typical mudrocks where radius ratios are <
675 4.4, a small grain between larger grains becomes too small to contact all neighboring large grains
676 (Zhou et al., 2016; de Frias Lopez et al., 2016).

677 For a grain pack with only small grains ($V_{\%L}$ = 0), the mean coordination number is
678 always less than 10 (Figure 11B), as there are no large grains with a high surface area for contact
679 and all the strong chains are made of small-small connections for all axial strains. As the large
680 grain concentration increases (0 < $V_{\%L}$ < 20), the interactions between the large and the small
681 grains begin increasing. The number of small grains is very high so the mean coordination
682 number for large grains considering all force chains (Figure 11A) ranges very high (~120 before
683 compaction; ~90 at final compaction). While majority of the strong force chains remain between
684 small grains (> 0.95) (Figure 12C), the small-large fraction of strong chains increases due to
685 grain interactions (Figure 12B). At even greater large grain concentrations (20 < $V_{\%L}$ < 70), the
686 mean coordination numbers (before and after compaction) decrease as the number of small
687 grains in the pack decrease (Figure 11). However, with increasing number of large grains, higher
688 interactions between large and small grains causes an increase in the small-large fraction of
689 strong chains (Figure 12B), since the vertical stress is transferred across the larger grains from
690 the grains above or below them. Similarly, as $V_{\%L}$ increases, the contacts between the large
691 grains also increase which causes an increase in the large-large fraction of strong chains (Figure
692 12C). However, as the grain matrix is made up of smaller grains, the large-large grain contacts
693 are much fewer in number than the small-large grain contacts, as seen in Figure 12D. At large
694 grain concentrations greater than 70%, the behavior changes drastically as the larger grains form
695 the matrix of the grain packs, and almost all the strong chains are formed across the large-large

contacts (Figure 12A), with a smaller fraction of small-large and small-small strong force chains (Figure 12B, C, D). The reduced number of small grains also decreases the mean coordination number (Figure 11).

Minh et al. (2014), de Frias Lopez et al. (2016), and Gong and Liu (2017) studied the force transmission and grain fabric of binary mixtures using three-dimensional DEM compression simulations for civil engineering studies. Based on the different contact type contributions to strong force chains as a function of the large grain concentrations, they observed cases for the grain packs similar to Figure 12D. Gong et al. (2019) also observed that after sustained compaction, the contribution of small-large fraction of force chains increased, while the small-small and large-large fraction decreased. Li and Wong (2016) conducted experiments and simulations of mudrock compaction. Their 2D finite element compaction simulations showed that for samples with low clay concentrations, there is strong stress concentration on the non-clay minerals and for samples with high clay volume fractions, the vertical stress and fabric orientation was more uniformly distributed. Thus, the concentration and distribution of different grain sizes plays a key role in the pore and throat size changes during compaction. It may prove useful to conduct reconsolidation experiments with different amounts of compression and grain concentrations to compare them with the simulation results.

6.0 Conclusion

Understanding the properties at the grain and pore scale that influence capillary entry pressure is an important component of risk assessment and prospect evaluation. Prediction of permeability is especially difficult in mudrocks as the sediments are typically a heterogeneous mixture made of different grains shapes and sizes (Daigle and Screaton, 2015). In this study, capillary pressure curves and permeability were simulated for multiple cases each of numerous

bidisperse spherical grain packs with varying radius ratios (10:1, 7:1, 5:1, 2:1) and concentrations both, with and without considering the effect of gravitational force and compaction on the grain packs. Moreover, simulations were also conducted for grain packs with ellipsoidal clay grains to mimic mudrocks better. The wide variety of cases ensured that effects of different variables on the petrophysics were captured in a comprehensive manner. Our simulations assume regular grain shapes such as spheres and ellipsoids for reducing simulation time and complexity. Since our simulations do not account for osmotic, electrical, or geochemical forces, it can create some deviations from experimental results. However, our work is directed towards studying the influence of grain size, shape, and distribution in mudrocks on fluid flow, without considering cementation or low porosity rocks. Hence, our grain packs serve as adequate representations for natural mudrocks despite these limitations.

Regardless of the changes in variables, all simulation results showed that on successive increase of larger spheres (silt grains) in a grain pack, the capillary pressure curves displayed two percolation thresholds, probably due to larger pore throats being sheltered adjacent to larger grains because of silt bridging. This was confirmed from the DEM simulations that showed that on increasing large grain concentration in the grain packs even before the matrix transition to large grains, there is formation of strong force chains across large-large and small-large grain contacts during compaction. This decreases the coordination numbers of the grains and shields the larger pores. However, this is only observed up to a certain stress limit (limited compaction), beyond which the increasing axial stress overwhelms the silt-bridging effect and the larger pores begin to collapse. It was also observed that at low values of larger grain concentrations, the smaller pore network did not let the invading fluid percolate across the grain pack, which preserves integrity of the mudrock seal. However, on sufficiently increasing the larger grain

concentration (40 – 60 $V_{\%L}$), the larger pore-throat system lowers the capillary percolation threshold, which allows the non-wetting fluid to flow through the grain pack. This can therefore cause seal failure even below the fracture pressure during CO_2 sequestration or hydrocarbon exploration. For example, the CO_2 plume in the Sleipner storage project ascended through eight thinner shales before being trapped under a thicker seal (Cavanagh and Haszeldine, 2014). The fluid migration was interpreted as a gravity driven percolation aided by low breakthrough pressures, microfractures and rock heterogeneity. The caprock samples collected at ~900 meters below seafloor had a concentration of 40 - 45 % silt-size grains with a porosity of 0.34 - 0.36 (Springer and Lindgren, 2006), which is similar to the disadvantageous seal properties caused by silt bridging.

Therefore, knowledge of the compaction, silt concentration, and grain size in mudrock seals, can make it possible to estimate the extent of silt bridging in the mudrock and thus, better quantify the sealing capacity. Understanding this phenomenon better will help advance our knowledge of pore systems and fluid flow in shales and mudrocks. Ultimately, this may affect risk management efforts during petroleum exploration or carbon sequestration by providing a more accurate understanding of seal quality.

7.0 Acknowledgements

We are grateful to Dr. Maša Prodanović for the invasion percolation code, and the Delaunay tessellation code and, to Trikon Technologies Inc. for providing an evaluation version of GeoDict. Funding was provided by the University of Texas at Austin and Equinor through the Statoil (Equinor) Fellowship program.

8.0 Data Availability

The datasets (bidisperse grain packs formed under gravity) used in this paper are stored on the Digital Rocks Portal (Bihani & Daigle, 2019b). The code created for the constant rate-of-strain uniaxial consolidation test (LIGGGHTS) and post-processing (MATLAB) is preserved on Zenodo (Bihani and Daigle, 2020), and a copy is also available in a GitHub repository at https://github.com/abhishekdbihani/compaction_LIGGGHTS.

9.0 References

Al-Raoush, R., Thompson, K., & Willson, C. S. (2003). Comparison of network generation techniques for unconsolidated porous media. Soil Science Society of America Journal, 67(6), 1687-1700.

Allen, J. (1985). Principles of physical sedimentology.272pp., Allen and Unwin, Winchester, Mass.

Amann-Hildenbrand, A., Krooss, B. M., Harrington, J., Cuss, R., Davy, C., Skoczylas, F., ... & Maes, N. (2015). Gas transfer through clay barriers. In Developments in Clay Science (Vol. 6, pp. 227-267). Elsevier.

Behseresht, J., Bryant, S. L., & Sepehrnoori, K. (2009). Infinite-Acting Physically Representative Networks for Capillarity-Controlled Displacements. SPE Journal, 14(4), 568–578. http://doi.org/10.2118/110581-pa

Bihani, A., & Daigle, H. (2019a). On the role of spatially correlated heterogeneity in determining mudrock sealing capacity for CO2 sequestration. Marine and Petroleum Geology, 106(106), 116–127. https://doi.org/10.1016/j.marpetgeo.2019.04.038

Bihani, A., & Daigle, H. (2019b). Bidisperse sphere packs generated under gravity [Data set]. Digital Rocks Portal. http://doi.org/10.17612/P74T20

786 Bihani, A., & Daigle, H. (2020, September 9). Uniaxial Compaction and Force-chain Analysis
787 of Bidisperse Grain Packs (Version v1.0). Zenodo.
788 http://doi.org/10.5281/zenodo.4021433
789 Blunt, M. J. (2017). Multiphase Flow in Permeable Media A Pore-Scale Perspective. Cambridge
790 University Press. http://doi.org/10.1017/9781316145098
791 Bryant, S. L., Mellor, D. W., & Cade, C. A. (1993). Physically representative network models of
792 transport in porous media. AIChE Journal, 39(3), 387–396.
793 http://doi.org/10.1002/aic.690390303
794 Cavanagh, A. J., & Haszeldine, R. S. (2014). The Sleipner storage site: Capillary flow modeling
795 of a layered CO2 plume requires fractured shale barriers within the Utsira Formation.
796 International Journal of Greenhouse Gas Control, 21, 101-112.
797 Clarke, R. H., Reservoir properties of conglomerates and conglomeratic sandstones, AAPG
798 Bull., 63, 799-809, 1979.
799 Crawford, B. R., Faulkner, D. R., & Rutter, E. H. (2008). Strength, porosity, and permeability
800 development during hydrostatic and shear loading of synthetic quartz-clay fault gouge.
801 Journal of Geophysical Research: Solid Earth, 113(B3).
802 Curtis, C. D., Lipshie, S. R., Oertel, G., & Pearson, M. J. (1980). Clay orientation in some Upper
803 Carboniferous mudrocks, its relationship to quartz content and some inferences about
804 fissility, porosity and compactional history. Sedimentology, 27(3), 333-339.
805 Daigle, H., & Reece, J. S. (2015). Permeability of Two-Component Granular Materials.
806 Transport in Porous Media, (October 2014), 523–544. http://doi.org/10.1007/s11242-014-
807 0412-6

808 Daigle, H., and Screaton, E. J. (2015), Predicting the permeability of sediments entering
809 subduction zones, Geophys. Res. Lett., 42,5219–5226, doi:10.1002/ 2015GL064542.
810 Daigle, H., Cook, A., and Malinverno, A. (2015), Permeability and porosity of hydrate-bearing
811 sediments in the northern Gulf of Mexico, Marine and Petroleum Geology, 68(A), 551-
812 564. https://doi.org/10.1016/j.marpetgeo.2015.10.004
813 Dawson, W. C., & Almon, W. R. (2002). Top Seal Potential of Tertiary Deep-water Gulf of
814 Mexico Shales. Gulf Coast Association of Geological Societies Transactions, 52, 167–
815 176. Retrieved from http://archives.datapages.com/data/gcags/data/052/052001/0167.htm
816 Day-Stirrat, R. J., Dutton, S. P., Milliken, K. L., Loucks, R. G., Aplin, A. C., Hillier, S., & van
817 der Pluijm, B. A. (2010). Fabric anisotropy induced by primary depositional variations in
818 the silt: clay ratio in two fine-grained slope fan complexes: Texas Gulf Coast and
819 northern North Sea. Sedimentary Geology, 226(1-4), 42-53.
820 Day-Stirrat, R. J., Schleicher, A. M., Schneider, J., Flemings, P. B., Germaine, J. T., & van der
821 Pluijm, B. A. (2011). Preferred orientation of phyllosilicates: Effects of composition and
822 stress on resedimented mudstone microfabrics. Journal of Structural Geology, 33(9),
823 1347–1358. https://doi.org/10.1016/j.jsg.2011.06.007
824 de Frias Lopez, R., Silfwerbrand, J., Jelagin, D., & Birgisson, B. (2016). Force transmission and
825 soil fabric of binary granular mixtures. Géotechnique, 66(7), 578-583.
826 Deng, X., & Davé, R. N. (2017). Properties of force networks in jammed granular media.
827 Granular Matter, 19(2), 27.
828 Desbois, G., Urai, J. L., & Kukla, P. A. (2009). Morphology of the pore space in claystones–
829 evidence from BIB/FIB ion beam sectioning and cryo-SEM observations. eEarth
830 Discussions, 4(1), 1-19.

GeoDict User Guide. (2017). Glatt E., Becker J., Wiegmann A., Planas B. GrainGeo Release 2017. MATH2MARKET GMBH. www.math2market.com

Gong, J., & Liu, J. (2017). Mechanical transitional behavior of binary mixtures via DEM: effect of differences in contact-type friction coefficients. Computers and Geotechnics, 85, 1-14.

Gong, J., Liu, J., & Cui, L. (2019). Shear behaviors of granular mixtures of gravel-shaped coarse and spherical fine particles investigated via discrete element method. Powder Technology, 353, 178-194.

Guiltinan, E. J., Espinoza, D. N., Cockrell, L. P., & Cardenas, M. B. (2018). Textural and compositional controls on mudrock breakthrough pressure and permeability. Advances in Water Resources, 121(August), 162–172. http://doi.org/10.1016/j.advwatres.2018.08.014

Heling, D. (1970). Micro-Fabrics of Shales and their Rearrangement by Compaction. Sedimentology, 15(3–4), 247–260. http://doi.org/10.1111/j.1365-3091.1970.tb02188.x

Hildenbrand, A., Schlömer, S., & Krooss, B. M. (2002). Gas breakthrough experiments on fine-grained sedimentary rocks. Geofluids, 2(1), 3–23. http://doi.org/10.1046/j.1468-8123.2002.00031.x

Ingram, G. M., Urai, J. L., & Naylor, M. A. (1997). Sealing processes and top seal assessment. Hydrocarbon Seals: Importance for Exploration and Production, pp 165-174, Norwegian Petroleum Society Special Publications. http://doi.org/10.1016/S0928-8937(97)80014-8

Jain, A. K., & Juanes, R. (2009). Preferential mode of gas invasion in sediments: Grain-scale mechanistic model of coupled multiphase fluid flow and sediment mechanics. Journal of Geophysical Research: Solid Earth, 114(8), 1–19. http://doi.org/10.1029/2008JB006002

852 Kloss, C., Goniva, C., Hager, A., Amberger, S., & Pirker, S. (2012). Models, algorithms and
853 validation for opensource DEM and CFD–DEM. Progress in Computational Fluid
854 Dynamics, an International Journal, 12(2-3), 140-152.
855 Koltermann, C., & Gorelick, S. M. (1995). Fractional packing model for hydraulic conductivity
856 derived from sediment mixtures. Water Resources Research, 31(12), 3283–3297.
857 http://doi.org/10.1029/95WR02020
858 Krushin, J. T. (1997). AAPG Memoir 67: Seals, Traps, and the Petroleum System. Chapter 3:
859 Seal Capacity of Nonsmectite Shale.
860 Li, B., & Wong, R. C. K. (2016). Quantifying structural states of soft mudrocks. Journal of
861 Geophysical Research: Solid Earth, 121(5), 3324-3347.
862 Mackay, A. L. (1973). To find the largest sphere which can be inscribed between four others.
863 Acta Crystallographica Section A, 29(3), 308–309.
864 http://doi.org/10.1107/S0567739473000768
865 Majmudar, T. S., & Behringer, R. P. (2005). Contact force measurements and stress-induced
866 anisotropy in granular materials. Nature, 435(7045), 1079-1082.
867 Marion, D. P., (1990). Acoustic, mechanical, and transport properties of sediments and granular
868 materials: Ph.D. dissertation, Stanford University.
869 Marion, D., Nur, A., Yin, H., & Han, D. H. (1992). Compressional velocity and porosity in sand-
870 clay mixtures. Geophysics, 57(4), 554-563.
871 Mason, G., & Mellor, D. (1995). Simulation of drainage and imbibition in a random packing of
872 equal spheres. Journal of Colloid and Interface Science, 225, 214–225.
873 http://doi.org/10.1006/jcis.1995.0024

874 Minh, N. H., Cheng, Y. P., & Thornton, C. (2014). Strong force networks in granular mixtures.
875 Granular Matter, 16(1), 69-78.
876 Oertel, G. (1983). The relationship of strain and preferred orientation of phyllosilicate grains in
877 rocks—a review. Tectonophysics, 100(1-3), 413-447.
878 Peters, J. F., Muthuswamy, M., Wibowo, J., & Tordesillas, A. (2005). Characterization of force
879 chains in granular material. Physical review E, 72(4), 041307.
880 Pommer, M., & Milliken, K. (2015). Pore types and pore-size distributions across thermal
881 maturity, Eagle Ford Formation, southern Texas. AAPG Bulletin, 99(9), 1713-1744.
882 Radjai, F., & Roux, S. (1995). Friction-induced self-organization of a one-dimensional array of
883 particles. Physical Review E, 51(6), 6177.
884 Radjai, F., Wolf, D. E., Jean, M., & Moreau, J. J. (1998). Bimodal character of stress
885 transmission in granular packings. Physical review letters, 80(1), 61.
886 Revil, A., & Cathles, L. M. (1999). Permeability of shaly sands. Water Resources Research,
887 35(3), 651–662.
888 Revil, A., Pezard, P. A. A., & de Larouzière, F. D. D. (1999). Fluid overpressures in western
889 Mediterranean sediments, Sites 974-979. Proc. Ocean Drill. Program, 161 Sci. Results,
890 161, 117–128. http://doi.org/10.2973/odp.proc.sr.161.274.1999
891 Sánchez-Arévalo, F. M., Tapia-McClung, H., Pulos, G., & Zenit, R. (2013). Reduction of
892 compaction force in a confined bidisperse granular media. Physical Review E, 87(5),
893 052210.
894 Schlömer, S., Krooss, B.M., (1997). Experimental characterisation of the hydrocarbon sealing
895 efficiency of cap rocks. Mar. Petrol. Geol. 14 (5), 565–580.

Schieber, J. (2010). Common Themes in the Formation and Preservation of Intrinsic Porosity in Shales and Mudstones – Illustrated with Examples Across the Phanerozoic. Society of Petroleum Engineers Unconventional Gas Conference, SPE Paper 132370, 10. http://doi.org/10.2118/132370-MS

Schneider, J., Flemings, P. B., Day-Stirrat, R. J., & Germaine, J. T. (2011). Insights into pore-scale controls on mudstone permeability through resedimentation experiments. Geology, 39(11), 1011–1014. http://doi.org/10.1130/G32475.1

Schowalter, T. T. (1979). Mechanics of secondary hydrocarbon migration and entrapment. AAPG Bulletin, 63(5), 723-760. https://doi.org/10.1306/2F9182CA-16CE-11D7-8645000102C1865D

Shakoor, A., & Cook, B. D. (1990). The effect of stone content, size, and shape on the engineering properties of a compacted silty clay. Bulletin of the Association of Engineering Geologists, 27(2), 245-253.

Song, J., & Zhang, D. (2013). Comprehensive review of caprock-sealing mechanisms for geologic carbon sequestration. Environmental Science and Technology, 47(1), 9–22. http://doi.org/10.1021/es301610p

Springer, N., & Lindgren, H. (2006, June). Caprock properties of the Nordland Shale recovered from the 15/9-A11 well, the Sleipner area. In 8th Greenhouse Gas Control Technologies conference (GHGT-8), Trondheim.

Thane, C.G. (2006). Geometry and Topology of Model Sediments and Their Influence on Sediment Properties. MS thesis, University of Texas at Austin, Austin, Texas.

Tordesillas, A. (2007). Force chain buckling, unjamming transitions and shear banding in dense granular assemblies. Philosophical Magazine, 87(32), 4987-5016.

Tordesillas, A., & Muthuswamy, M. (2009). On the modeling of confined buckling of force chains. Journal of the Mechanics and Physics of Solids, 57(4), 706-727.

Torskaya T. (2013). Pore-Scale Analysis of Grain Shape and Sorting Effects on Fluid Transport Phenomena in Porous Media. PhD Dissertation, University of Texas at Austin, Austin, Texas.

Velde, B. (1996). Compaction trends of clay-rich deep sea sediments. Marine Geology, 133(3–4), 193–201. https://doi.org/10.1016/0025-3227(96)00020-5.

Washburn E.W. (1921) Note on a method of determining the distribution of pore sizes in a porous material. Proceedings of the National Academy of Science, 115–116.

Watts, N. L. (1987). Theoretical aspects of cap-rock and fault seals for single- and two-phase hydrocarbon columns. Marine and Petroleum Geology, 4(4), 274–307. http://doi.org/10.1016/0264-8172(87)90008-0

Wu, K., Remond, S., Abriak, N., Pizette, P., Becquart, F., & Liu, S. (2017). Study of the shear behavior of binary granular materials by DEM simulations and experimental triaxial tests. Advanced Powder Technology, 28(9), 2198-2210.

Yang, Y., & Aplin, A. C. (2007). Permeability and petrophysical properties of 30 natural mudstones. Journal of Geophysical Research: Solid Earth, 112(B3).

Yang, Y., Aplin, A.C., 2010. A permeability-porosity relationship for mudstones. Mar. Petrol. Geol. 27 (8), 1692–1697. https://doi.org/10.1016/j.marpetgeo.2009.07.001

Zhou, W., Xu, K., Ma, G., Yang, L., & Chang, X. (2016). Effects of particle size ratio on the macro-and microscopic behaviors of binary mixtures at the maximum packing efficiency state. Granular Matter, 18(4), 81.